



# Antisymmetric oscillation modes in rectangular screeching jets

Romain Gojon, Ephraim Gutmark, Mihai Mihaescu

## ► To cite this version:

Romain Gojon, Ephraim Gutmark, Mihai Mihaescu. Antisymmetric oscillation modes in rectangular screeching jets. *AIAA Journal*, 2019, 57 (8), pp.3422-3441. 10.2514/1.J057514 . hal-03162269

**HAL Id: hal-03162269**

**<https://hal.science/hal-03162269>**

Submitted on 8 Mar 2021

**HAL** is a multi-disciplinary open access archive for the deposit and dissemination of scientific research documents, whether they are published or not. The documents may come from teaching and research institutions in France or abroad, or from public or private research centers.

L'archive ouverte pluridisciplinaire **HAL**, est destinée au dépôt et à la diffusion de documents scientifiques de niveau recherche, publiés ou non, émanant des établissements d'enseignement et de recherche français ou étrangers, des laboratoires publics ou privés.



## Open Archive Toulouse Archive Ouverte

OATAO is an open access repository that collects the work of Toulouse researchers and makes it freely available over the web where possible

This is an author's version published in: <http://oatao.univ-toulouse.fr/27049>

### Official URL:

<https://doi.org/10.2514/1.J057514>

### To cite this version:

Gojon, Romain and Gutmark, Ephraim and Mihaescu, Mihai  
*Antisymmetric oscillation modes in rectangular screeching jets*. (2019) AIAA Journal, 57 (8). 3422-3441. ISSN 1533-385X

Any correspondence concerning this service should be sent  
to the repository administrator: [tech-oatao@listes-diff.inp-toulouse.fr](mailto:tech-oatao@listes-diff.inp-toulouse.fr)

# Antisymmetric oscillation modes in rectangular screeching jets

Romain Gojon<sup>1,\*</sup>, Ephraim Gutmark<sup>2,†</sup> and Mihai Mihaescu<sup>3,‡</sup>

*1. ISAE-SUPAERO*

*Université de Toulouse*

*Toulouse, France*

*2. Department of Aerospace Engineering & Mechanics*

*University of Cincinnati*

*Cincinnati, OH, United States*

*3. Department of Mechanics, Royal Institute of Technology (KTH)*

*Linné FLOW Centre*

*Stockholm, Sweden*

In this paper, the origin and the properties of the oscillation modes in screeching non-ideally expanded rectangular jets are investigated using compressible implicit LES of rectangular supersonic jets. At the exit of a converging diverging rectangular nozzle of aspect ratio 2 and of design Mach number 1.5, the jets are under- and over-expanded. Seven simulations with four different temperature ratios ranging from 1 to 3 and two different nozzle pressure ratios are performed. The geometry of the nozzle and the exit conditions are chosen such that to match the experimental study conducted at the University of Cincinnati. First, the over-expanded jets are studied. It is shown that the total number of shock cells decreases with increased temperature ratio. However, the temperature does not influence the size of the first shock cell and the linear decrease of the shock cell size in the downstream direction. The spreading of the jet is observed to be higher along the minor axis plane than along the major axis plane. The intensity of the screech noise increases with the temperature ratio in the present study although the opposite is observed in the experiments. Moreover, for jet temperature ratios of 2.5 and 3, the strong flapping motion of the jet along the minor axis plane due to the screech feedback mechanism yields to an antisymmetric organization of the Mach wave radiation. Thereafter, the near- and far-field acoustic are studied. In the near-field, screech tones are captured, whose frequencies are consistent with both experimental data and theoretical models. In the far-field, four acoustic components typical of non-ideally expanded supersonic jets are observed, namely the screech noise, the broadband shock-associated noise, the mixing noise and the Mach wave noise. Their directivities and frequencies are in agreement with experimental results and models. The mechanism of the screech noise generation is studied by using a Fourier decomposition of the pressure field. For the four over-expanded jets, a flapping motion along the diagonal or along the minor axis plane of the jet is noted. Finally, the hypothesis that the acoustic waves completing the feedback loop in these jets are linked to the upstream-propagating acoustic wave modes of the equivalent ideally expanded jets is tested. Using a jet vortex sheet model to describe the dispersion relations of these modes, it is found that this hypothesis allows us to explain the antisymmetric jet oscillation observed at the screech frequencies. Based on frequency-wavenumber decomposition of the pressure fluctuations in the jets, it is shown that at the screech frequencies, acoustic waves propagating in the upstream direction at the ambient speed of sound exist also in the jet flow, additionally

---

\*Research associate, AIAA Member, romain.gojon@isae-supaero.fr

†Distinguished Professor, Fellow AIAA, gutmarej@ucmail.uc.edu

‡Associate Professor, Senior Member AIAA, mihai@mech.kth.se

to the acoustic waves propagating outside of the jet. These acoustic waves belong to the neutral acoustic wave modes of the equivalent ideally expanded jet. These results support the idea that a vortex sheet model of the corresponding 2-D planar ideally expanded jet is capable of predicting the wave modes of a non-ideally expanded rectangular supersonic jet. They also suggest that these waves are involved in the feedback part of the screech mechanism; explaining why, for the simulated screeching rectangular jets, the associated oscillation mode is antisymmetric.

## Nomenclature

$\delta$	=	half velocity width of the jet ( $m$ )
$\theta$	=	angle of observation (degrees)
$\mu_j$	=	viscosity in the ideally expanded jet, computed using Sutherland's Law ( $kg.(m.s)^{-1}$ )
$\nu_j = \mu_j/\rho_j$	=	kinematic viscosity in the ideally expanded jet ( $m^2.s^{-1}$ )
$\omega$	=	frequency ( $rad.s^{-1}$ )
$\rho_j$	=	density in the ideally expanded equivalent jet ( $kg.m^{-3}$ )
$a_0$	=	speed of sound in the ambient ( $m.s^{-1}$ )
$a_j$	=	speed of sound in the ideally expanded equivalent jet ( $m.s^{-1}$ )
$A_d = 2h \times h$	=	exit area of the nozzle ( $m^2$ )
$A_j$	=	exit area of the ideally expanded equivalent nozzle ( $m^2$ )
$b$	=	depth of the nozzle ( $m$ )
$b_j$	=	depth of the ideally expanded equivalent nozzle ( $m$ )
$D_{eq} = \sqrt{8/\pi}h$	=	equivalent exit diameter of the jet ( $m$ )
$f$	=	frequency ( $Hz$ )
$h$	=	height of the nozzle ( $m$ )
$h_j$	=	height of the ideally expanded equivalent nozzle ( $m$ )
$k$	=	wavenumber ( $rad.m^{-1}$ )
$L_n$	=	length of the n-th shock cell ( $m$ )
$L_s$	=	length of the first shock cell ( $m$ )
$L_{sh}$	=	length scale related to the shock cell size ( $m$ )
$\mathcal{M}_c$	=	convective Mach number
$\mathcal{M}_d$	=	design Mach number of the jet
$\mathcal{M}_j$	=	Mach number of the ideally expanded equivalent jet
$n$	=	mode number of the oscillation mode of the planar jet
$Re = u_j D_{eq}/\nu_j$	=	Reynolds number
$u_c$	=	convection velocity ( $m.s^{-1}$ )
$u_j$	=	velocity of the ideally expanded equivalent jet ( $m.s^{-1}$ )
$St = f D_{eq}/u_j$	=	Strouhal number based on $D_{eq}$
$St_{h_j} = f h_j/u_j$	=	Strouhal number based on $h_j$
$x$	=	coordinate along the major axis of the nozzle ( $m$ )
$y$	=	coordinate along the minor axis of the nozzle ( $m$ )
$z$	=	coordinate along the jet axis ( $m$ )

## I. Introduction

Rectangular propulsion systems closely integrated with the fuselage are considered for modern high-speed aircraft. Supersonic non-ideally expanded jets exiting from such geometries can lead to very intense acoustic noise. Several acoustic components can be observed including, mixing noise, broadband shock-associated noise, Mach wave noise and screech noise [1]. In non-ideally expanded jets, a specific asymmetric shock pattern is observed [2] but the main acoustic sources are the same as the ones for round jets [3].

Mixing noise is observed in both subsonic [4] and supersonic [3] jets. The directivity of this noise component is strongest around angles of 160 degrees with respect to the upstream direction and its dominant Strouhal number based on the nozzle exit equivalent diameter and the jet ideally expanded velocity is around 0.2. This component is mainly generated at the end of the potential core [5–7]. For subsonic jets, Bogey and Bailly [5] proposed that this acoustic component is due to the intermittent intrusion of turbulent structures into the potential core.

Broadband shock-associated noise (BBSAN) is produced by the interactions between the turbulent structures in the jet shear layers and the shock cell structure. In his pioneering work, Martlew [8] identified BBSAN. Several other experiments were conducted [9–11] and the central frequency of this noise component was found to vary with the directivity angle in the far field. Harper-Bourne and Fisher [12] built a model which predicts the central frequency of this noise component as a function of the observation angle.

When turbulent structures in the jet shear layers are convected at a supersonic speed, they produce Mach wave radiation. The Mach waves are observed as shocks attached to a supersonic traveling feature. Its directivity is given by the model of Oertel [13].

The screech noise is due to an aeroacoustic feedback between acoustic waves propagating upstream and turbulent structures convected downstream. This mechanism was described by Powell [14] and reviewed by Raman [15] and consists of two steps. First, the turbulent structures developing in the jet shear layer and convecting in the downstream direction interact with the quasi-periodic shock cell structure of the jet, creating upstream propagating acoustic waves. The resonance loop is closed at the trailing edge of the nozzle where the jet shear layer is excited when the upstream propagating acoustic waves impinge on the nozzle lips. At the screech tone frequencies, the jets undergo strong oscillations.

For round jets, Powell [14] identified four oscillation modes,  $A$ ,  $B$ ,  $C$ , and  $D$ , on the basis of the variations of the screech frequency with the jet ideally expanded Mach number  $\mathcal{M}_j$ . Each mode is observed over a specific range of Mach number, and frequency jumps are noted between the modes. Later, Merle [16] showed that the mode  $A$  can be divided into modes  $A1$  and  $A2$ . Davies and Oldfield [17] studied the oscillation modes of the jets associated with the screech modes. They found that the modes  $A1$  and  $A2$  correspond to axisymmetric oscillation modes, the mode  $C$  to helical modes, and the modes  $B$  and  $D$  to flapping and sinuous modes. For round jets, an explanation of the oscillation modes of the jet is proposed in a previous paper [18].

For rectangular jets, Raman and Rice [19] were the first to observe that the screech feedback mechanism was always associated with a flapping motion of the jet along the smaller dimension of the jet. They used a convergent rectangular nozzle of aspect ratio 9.63. In this paper, the origin of the oscillation modes of screeching rectangular jets is investigated, assuming that the feedback part of the aeroacoustic loop responsible for screech noise is related to the neutral acoustic wave modes of the equivalent ideally expanded jets.

In the current study, we investigate a supersonic jet exiting from a 2:1 aspect ratio rectangular convergent-diverging nozzle at four different temperature conditions and two different nozzle pressure ratios. The impact of the jet temperature on the flow and the acoustic fields associated with such configurations is targeted. An experimental study of a similar jet is conducted at the University of Cincinnati [20]. The spectral and hydrodynamic properties of the jet are described and compared with experimental data and models. A modified artificial dissipation scheme, suitable for large-eddy simulations of highly compressible flows is employed and described in section II. The jet parameters and the numerical methods used for the simulations are presented in section III and a convergence study is performed in section IV. The aerodynamic and acoustic results are presented in sections V and VI, respectively. The oscillation mode of the jets at the screech frequency is then discussed in section VII. In section VIII, we assume that the feedback part of the aeroacoustic loop responsible for screech noise is related to the neutral acoustic wave modes of the equivalent ideally expanded jets. First, such modes are characterized by a wave analysis using a vortex sheet model. Then, an attempt is made to detect upstream-propagating waves in screeching jets. Finally, concluding remarks are given in section IX.

## II. The flow solver

The compressible flow solver [21] has already been used in previous studies by Semlitsch *et al.* [22, 23] to perform Large Eddy Simulations of round non-ideally expanded supersonic jets. The simulations are carried out by using a finite volume method and by solving the unsteady compressible Navier-Stokes equations on

structured meshes. An explicit standard four-stage Runge-Kutta algorithm is used for time integration and a second order central difference scheme is used for spatial discretization. In order to improve the aeroacoustic capabilities of the solver, at the end of each time step, a modified artificial dissipation is added to the inviscid flows in order to remove grid-to-grid oscillations, to avoid Gibbs oscillations near shock and to relax subgrid-scale turbulent energy. The smallest sub-grid scale (SGS) flow structures not resolved by the grid are dissipated by the added artificial dissipation, in a similar way as explicit filtering in other studies [24–26].

This artificial dissipation has been designed in the same way that proposed by Jameson *et al.* [27] Moreover, in order to separate turbulent structures and shocks, a modification similar to the one proposed by Ducros *et al.* [28] has been used. The resulting dissipation added to the inviscid fluxes between two nodes, named 0 and 1, is

$$D_{01} = \left[ \epsilon_{01}^{(2)}(U_1 - U_0) - \epsilon_{01}^{(4)}(\Delta U_1 - \Delta U_0) \right] \phi_{01} r_{01} \quad (1)$$

where  $U_0$  is the vector containing the conservative variables at node 0,  $\epsilon_{01}^{(2)}$  and  $\epsilon_{01}^{(4)}$  are the dissipation functions,  $\Delta$  is the Laplacian operator,  $r_{01}$  is the spectral radius and  $\phi_{01}$  is a function depending on the grid stretching. Considering the surface  $S_{01}$  between the node 0 and the node 1, the averaged cell face speeds  $u_{i,01} = (u_{i,0} + u_{i,1})/2$  and the averaged cell face speed of sound  $c_{01} = (c_0 + c_1)/2$ , the spectral radius  $r_{01}$  writes

$$r_{01} = (|u_{i,01} n_{i,01}| + c_{01}) S_{01} \quad (2)$$

where  $n_{i,01}$  is the normal vector of the surface.

The function  $\phi_{01}$  then writes

$$\phi_{01} = 4 \frac{\phi_0 \phi_1}{\phi_0 + \phi_1} \text{ where } \phi_0 = \left( \frac{r_0}{4r_{01}} \right)^{0.3} \quad (3)$$

where  $r_0$  is the sum of all the spectral radii of the node 0.

The dissipation functions are

$$\begin{cases} \epsilon_{01}^{(2)} = \max(\epsilon_0^{(2)}, \epsilon_1^{(2)}) \\ \epsilon_{01}^{(4)} = (1/2 + 1/2 \min(\max(\Phi_0, \Phi_1), \max(\Theta_0, \Theta_1))) \max(0, C_4 - \epsilon_{01}^{(2)}) s_4 \end{cases} \quad (4)$$

with

$$\epsilon_0^{(2)} = C_2 \Phi_0 \left( \frac{|\sum p_k - p_0|}{\sum p_k + p_0} \right) s_2, \quad \Phi_0 = \frac{(\nabla \cdot u_0)^2}{(\nabla \cdot u_0)^2 + \omega^2} \text{ and } \Theta_0 = \frac{\omega^2}{(\nabla \cdot u_0)^2 + \omega^2}$$

where  $u_0$  is the velocity at the node 0,  $\omega$  is the vorticity,  $C_2$  and  $C_4$  are constants to define,  $p_0$  is the pressure in the node 0 and  $s_2 = 3(N_0 + N_1)/N_0 N_1$  and  $s_4 = s_2^2/4$  are scaling factors which permit to take into account the number of neighbours with  $N_0$  the number of neighbours of the node 0.  $\Phi_0$  varies between 0 for weakly compressible regions to about 1 in shock regions. The capabilities of this dissipation mechanism were assessed for three benchmark aeroacoustic test cases, namely an acoustic pulse, a shock propagation and a shock-vortex interaction. Based on this validation, the constants values were set to  $(C_2, C_4) = (1.5, 0.04)$ . The results for the three test cases can be found in Gojon *et al.* [29].

### III. Parameters of the study

#### III.A. Jet parameters

Compressible implicit Large Eddy Simulation calculations of a supersonic rectangular jet are performed for two different nozzle pressure ratios (NPR) of 3, 4 and four different temperature ratios (TR) of 1, 2, 2.5, and 3. The seven different cases are presented in Table 1. The jets originate from a rectangular converging-diverging nozzle of aspect ratio (AR) of 2 : 1, which has a height of  $h = 12.95\text{mm}$  in the minor axis plane. The design nozzle pressure ratio of this nozzle is 3.67, yielding a design Mach number of  $\mathcal{M}_d = 1.5$ . In this study, the jets are over-expanded when the nozzle pressure ratio is equal to 3 and under-expanded when the nozzle pressure ratio is equal to 4. Sutherland's law is used to compute the viscosity. The geometry and the operating conditions match those in the experimental study by Mora *et al.* [20] Please note that the experiments have been performed on two different occasions with different operating points. First, a PIV

setup has been used in order to have access to the aerodynamic fields in the minor and major axis planes for three operating conditions at  $NPR = 3$  and  $TR = 1$ ,  $TR = 2$  and  $TR = 2.5$ . Second, microphones have been used in the far-field to analyse the directivity of the noise emissions for six operating conditions at  $TR = 1$ ,  $TR = 2$  and  $TR = 3$  for nozzle pressure ratios of 3 and 4.

	$NPR$	$\mathcal{M}_j$	$TR$	$T_j$ (K)	$u_j$ (m.s <sup>-1</sup> )	$Re$
Jet3TR1	3	1.36	1.	214	398	$9.64 \times 10^5$
Jet3TR2	3	1.36	2.	428	563	$4.00 \times 10^5$
Jet3TR25	3	1.36	2.5	535	629	$3.04 \times 10^5$
Jet3TR3	3	1.36	3.	642	689	$2.48 \times 10^5$
Jet4TR1	4	1.56	1.	197	439	$1.24 \times 10^6$
Jet4TR2	4	1.56	2.	394	620	$5.09 \times 10^5$
Jet4TR3	4	1.56	3.	592	760	$3.14 \times 10^5$

Table 1. Jet parameters: Nozzle Pressure Ratio  $NPR$ , ideally expanded Mach number  $\mathcal{M}_j$ , Temperature Ratio  $TR$ , ideally-expanded jet temperature and velocity  $T_j$  and  $u_j$  and Reynolds number  $Re = u_j D_{eq} / \nu_j$ .

### III.B. Numerical parameters

Large Eddy Simulations are carried out using the compressible flow solver [21] with the artificial dissipation presented in section II. At the inlet of the nozzle, total pressure, total temperature and flow direction are specified. Based on the static pressure data extrapolated from the internal value, the flow velocity and the static temperature at the nozzle inlet are determined using standard isentropic relations. These values are then applied to the inlet boundary; the strong condition is used. On all the other boundaries, characteristic boundary conditions are applied in a weak formulation with target states for the static pressure, the static temperature and the velocity corresponding to ambient values  $P = 101325 Pa$ ,  $T = 293 K$  and  $u = 0 m.s^{-1}$ , respectively. Those conditions combined with the implementation of sponge zones, consisting of grid stretching, permit to avoid spurious reflections in the physical domain. Adiabatic no-slip conditions are used at the nozzle walls. Please note that no tripping strategy was used inside the nozzle as the boundary layer is already naturally tripped by the sharp angle between the converging and the diverging part of the nozzle and by shock-boundary layer interactions in the diverging part of the nozzle.

## IV. Convergence study

### IV.A. Parameters

A convergence study has been performed for the cold jet Jet3TR1. Three structured meshes consisting of 64 blocks were designed with 40, 80 and 160 million nodes, respectively. A visualization of the converging diverging nozzle along the minor axis plane is shown in Figure 1(a) picturing half the nozzle [20]. In Figure 1(b), the intermediate structured mesh along the same plane is represented. All the meshes have been designed in order to have a mesh size of  $y^+ \sim 1$  in the wall normal direction and of  $x^+ < 10$  in the wall parallel directions in the second half of the diverging part of the nozzle. In order to reach such discretization, the near-wall resolution at the nozzle exit is equal to  $0.0012h$  in the wall normal direction and  $0.012h$  in the wall parallel direction. Moreover, the stretching of the mesh is kept below 5% in the domain of interest to preserve numerical accuracy.

The main differences between the meshes are the mesh sizes close to the jet axis in the  $(x, y)$  plane, in the near acoustic field, and in the axial direction. Close to the mesh axis, the mesh size in the  $(x, y)$  plane is equal to  $0.024h$  for the 40 million nodes mesh,  $0.016h$  for the 80 million nodes mesh and  $0.01h$  for the 160 million nodes mesh. In the acoustic field, the cut-off Strouhal number  $St = f D_{eq} / u_j$  has been chosen equal to 1.6, 2.4 and 3 for the 40, 80 and 160 million nodes meshes where  $f$  is the frequency,  $D_{eq}$  is the equivalent diameter of the jet, and  $u_j$  is the ideally expanded jet velocity. The maximum allowable mesh sizes in the acoustic field are then computed considering a minimum amount of 11 grid cells per wave length needed to accurately propagate an acoustic wave with the considered solver. Maximum allowable mesh sizes of  $0.077h$ ,  $0.051h$  and  $0.041h$  are obtained for the 40, 80 and 160 million nodes meshes. Finally, in the axial direction, the mesh size increases faster for the 40 million nodes mesh than for the 160 million nodes one with values

going from  $0.055h$  for the first one to  $0.03h$  for the last one at  $z = 10h$ . In the physical domain, that is the computational domain without the sponge zones, the maximum aspect ratio decreases from 64 for the 40 million nodes mesh to 34 for the 160 million nodes one.

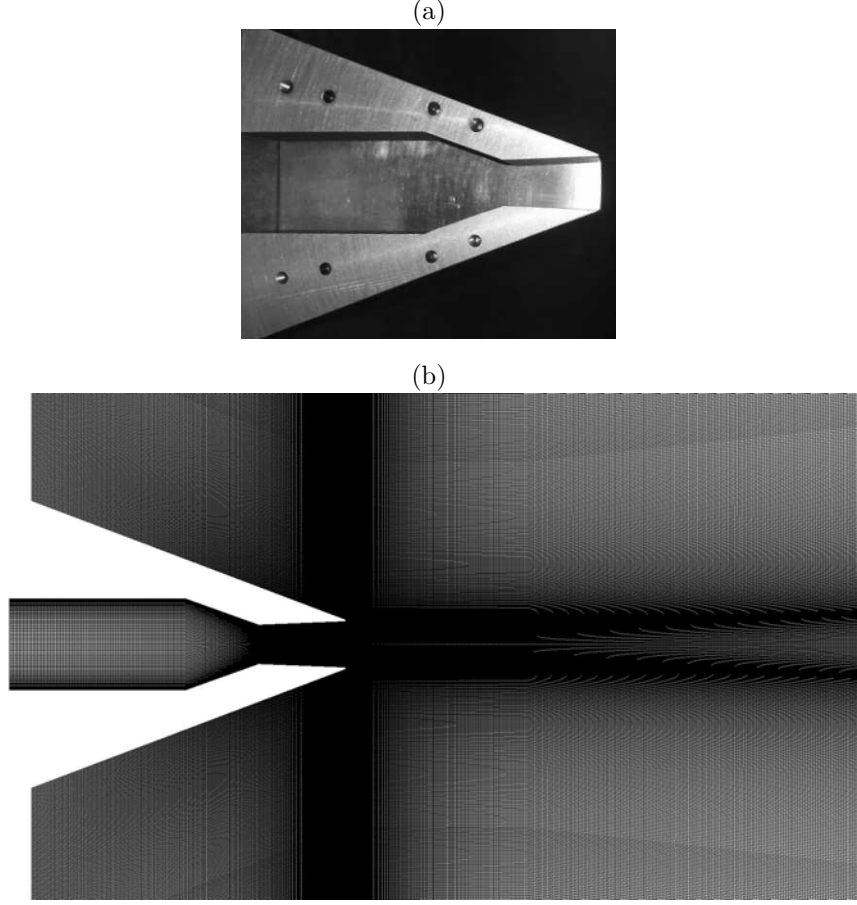


Figure 1. (a) Picture of half the nozzle showing the converging diverging geometry along the minor axis plane and (b) 80 million nodes structured mesh along the same plane.

#### IV.B. Results

Visualizations of the flow and near-field acoustics as calculated with two different grid resolutions, 40 and 160 million nodes are represented in Figure 2. The pressure fields along the major axis plane are also shown. Qualitatively, when the number of nodes increases, smaller structures are observed in the jet shear-layers and higher frequencies are propagated in the surrounding near acoustic field.

Data obtained with LES for the three different grid resolutions are compared in Figure 3 with experimental results along the jet axis and along the minor/major axis on the plane  $z = 2h$ . The shock-cell structure and the levels obtained in the LES and in the experiment are overall in good agreement. However, when increasing the number of nodes, the length of the shock cells follows better the experimental results.

At the nozzle exit, the mean axial velocity fields and the turbulence intensity are represented along the minor and the major axis in Figure 4. Along the minor axis plane, in Figure 4(a), the mean velocity profiles are similar. However, the overshoot visible at  $y = 0.47h$  is lower for the 160 million nodes LES than for the 40 million and the 80 million nodes LES. Moreover, for the 160 million nodes LES, a turbulent boundary-layer profile can be seen, with a momentum thickness of  $\delta_\theta = 0.08h$ . In Figure 4(b), it can be observed that the higher the number of grid points, the higher the turbulence intensity at the nozzle exit, from 1.05% for the 40 million nodes LES to 1.75% for the 160 million nodes LES. The results along the major axis plane are represented in Figure 4(c,d). The same conclusions as in the minor axis plane can be drawn for the mean velocity profiles. For the turbulence intensity, the level increases with the number of points in the boundary layer, at  $z = 0.98h$ . However, for the 80M and 160M LES, a second hump is visible around  $x = 0.92h$  and



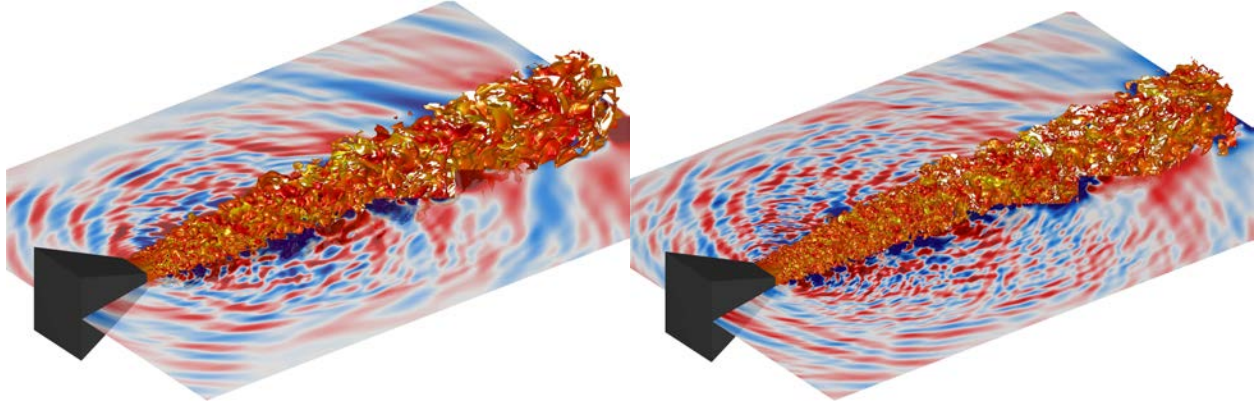


Figure 2. Isosurfaces of density for the cold jet Jet3TR1 with a (left) 40M nodes and (right) 160M nodes meshes. The isosurfaces for  $1.2 \text{ kg.m}^{-3}$  are represented colored by the Mach number. The pressure field along the major axis plane is also shown. The nozzle is in black.

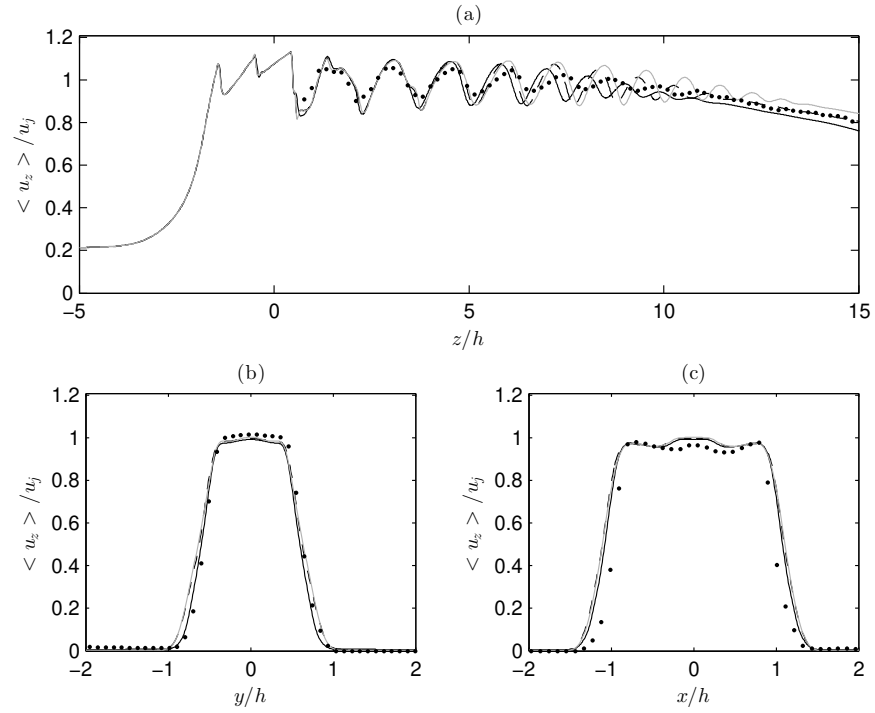


Figure 3. Mean axial velocity field for the cold jet Jet3TR1 along (a) the jet axis, (b) the minor axis at  $z = 2h$  and (c) the major axis at  $z = 2h$ ;  $\bullet$  PIV results and — 40M, - - - 80M and ..... 160M LES results.

its peak value decreases from 1.6% to 1.3% from the 80M to the 160M LES.

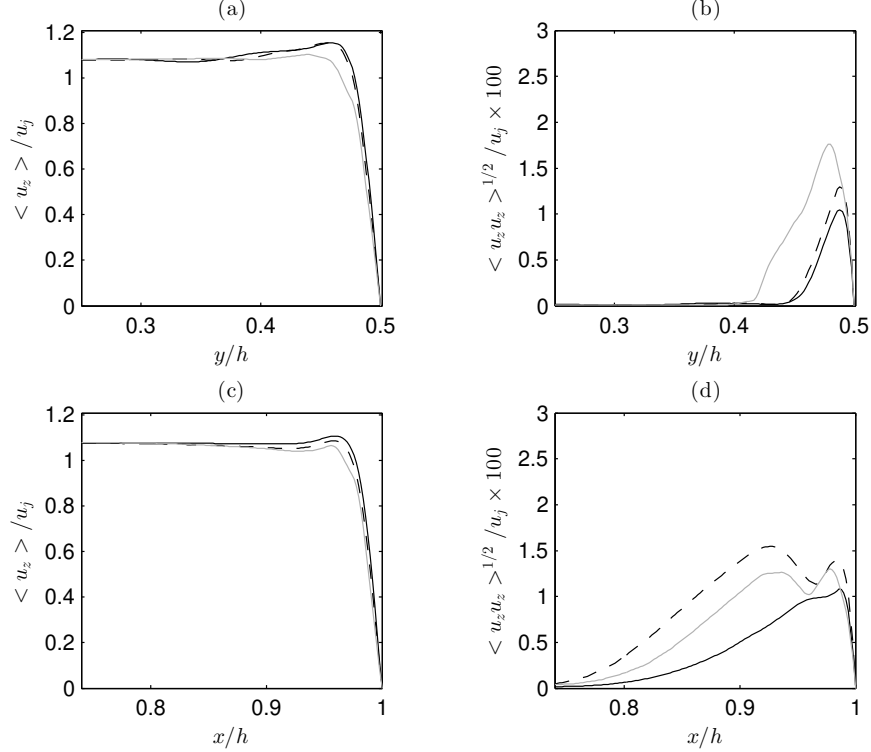


Figure 4. Mean axial velocity (a,c) and turbulence intensity (b,d) at the nozzle exit for the cold jet Jet3TR1 along (a,b) the minor axis plane, (c,d) the major axis plane; — 40M, --- 80M and — 160M LES results.

By looking at the turbulence levels inside the nozzle in Figure 5, it can be observed that elevated values of turbulence intensity at the nozzle exit are due to the interaction of the oblique shocks of the shock cell structure created by the sharp angle between the converging and the diverging part of the nozzle with the boundary layer inside the nozzle. It can be observed that the turbulence level increases in the boundary layer when passing through a shock. This is visible at  $z = -h$  in Figure 5(a) along the minor axis plane and at  $z = -1.4h$  in Figure 5(b) along the major axis plane. Moreover, the humps visible in Figure 4(a) for the 160M LES at  $y = 0.45h$  and the maximal values obtained at  $x = 0.92h$  for the 80M LES and the 160M LES are due to the oblique shock of the first cell of the shock cell structure created at the nozzle exit. The first oblique shock is not attached exactly to the nozzle trailing edge but to the inside of the nozzle at  $z = -0.05h$  in Figure 5(a) along the minor axis plane, and at  $z = -0.2h$  in Figure 5(b) along the major axis plane.

The mesh with 160 million nodes will be used in this study, as it permits to follow better the shock cell structure observed experimentally, to have higher turbulence intensity levels at the nozzle exit and to propagate higher frequencies in the near acoustic field.

## V. Flow field results

The seven LES simulations (see Table 1) are performed on the 160 million nodes mesh. A total of 400,000 time steps of  $\Delta t = 0.00125 D_{eq}/u_j$  are computed in each case after the transient period, permitting a simulation time of  $500 D_{eq}/u_j$  where  $D_{eq}$  is the equivalent diameter of the jet. This value is sufficient to analyse noise generation mechanism in jet noise. Nichols *et al.* [30] used a simulation time of  $45 D_{eq}/u_j$  to study the aeroacoustic features of a supersonic jet exiting from a rectangular aspect ratio 4 nozzle with an equivalent exit diameter  $D_{eq}$  and Bogey *et al.* [31] simulated total times of  $75 D/u_j$  and  $100 D/u_j$  to study the flow and acoustic fields of subsonic round jets of exit diameter  $D$ . More recently, with the increase of computing power, Lorteau *et al.* [32] and Bogey and Gojon [33] computed total simulation times of  $500 D_j/u_j$  and  $250 D_j/u_j$  in order to study the aeroacoustic characteristics of supersonic round jets and Gojon *et al.* [34] simulated  $500 h/u_j$  in order to study the feedback mechanism establishing in supersonic planar impinging jets of height  $h$ .

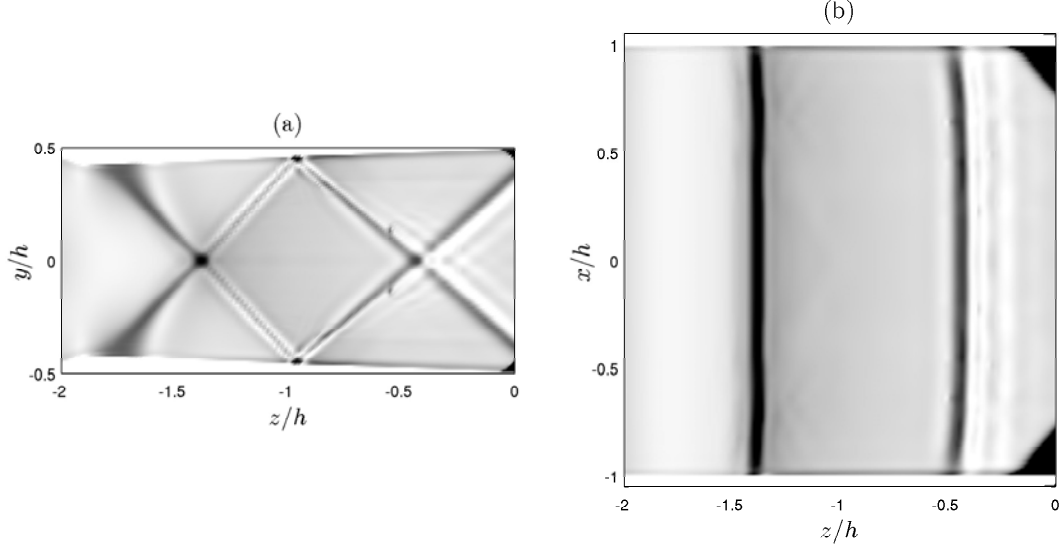


**Figure 5.** Turbulence intensity  $\langle u_z u_z \rangle^{1/2} / u_j$  (a) along the minor axis plane and (b) along the major axis plane inside the nozzle; 160M LES; Jet3TR1 results. The nozzle exit plane is located at  $z = 0$ . The colour scale ranges from white to black, from 0 to 1%.

### V.A. Instantaneous features

Snapshots along the minor axis plane for Jet3TR1 and Jet4TR1 are displayed in Figure 6, permitting to visualize simultaneously the jet flow and the acoustic field. It can be observed, by looking at the first cell of the shock cell structure, that Jet3TR1 and Jet4TR1 are respectively over-expanded and under-expanded, as expected for this nozzle whose design nozzle pressure ratio is 3.67.

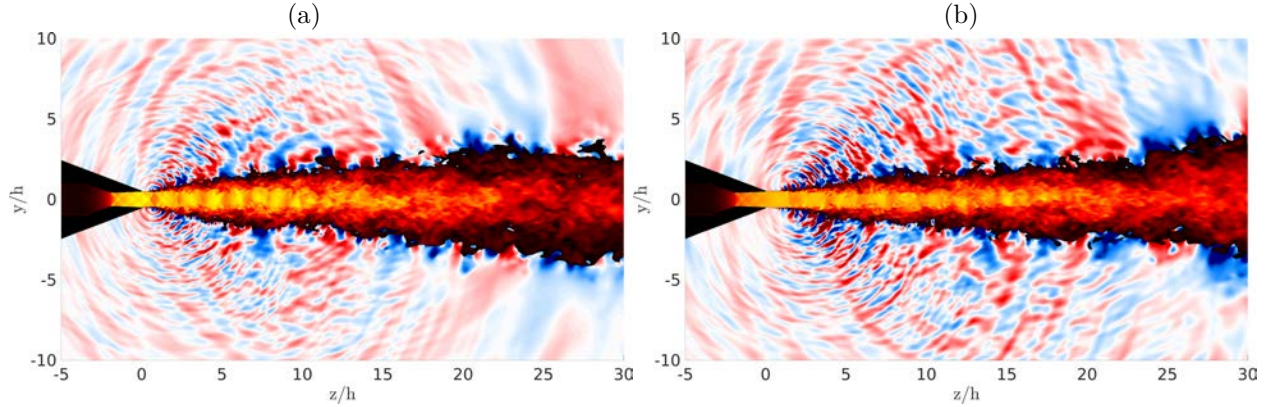


**Figure 6.** Snapshot along the minor axis plane representing the Mach number in the jet and the fluctuating pressure around for (a) Jet3TR1 and (b) Jet4TR1. The nozzle is in black.

In order to observe the influence of the temperature on the acoustic emissions of the jet, three-dimensional snapshots are displayed in Figure 7 for Jet3TR1, Jet3TR2 and Jet3TR3. The jet shear-layers are shown using isosurfaces of density and the near acoustic fields along the minor axis plane and along the major axis plane are represented using the instantaneous pressure. For Jet3TR1 and Jet3TR3, animations are proposed online to better visualize the evolution in time.

In Figure 7(a,b), for the cold jet ( $TR = 1$ ), three features are observed in the near acoustic field. First, acoustic waves propagating in the upstream direction in the vicinity of the nozzle are visible. These waves are linked to the screech noise. This noise component has been observed in various studies [14, 16, 17, 35, 36]. The second acoustic contribution that can be seen consists of circular acoustic waves emanating from the jet shear layers at different axial positions. These acoustic waves are due to the interactions between the turbulent structures and the shock cell structure in the jet shear-layers. Those interactions lead to the observation of broadband shock-associated noise in the far-field [10, 11, 37]. The third acoustic component visible



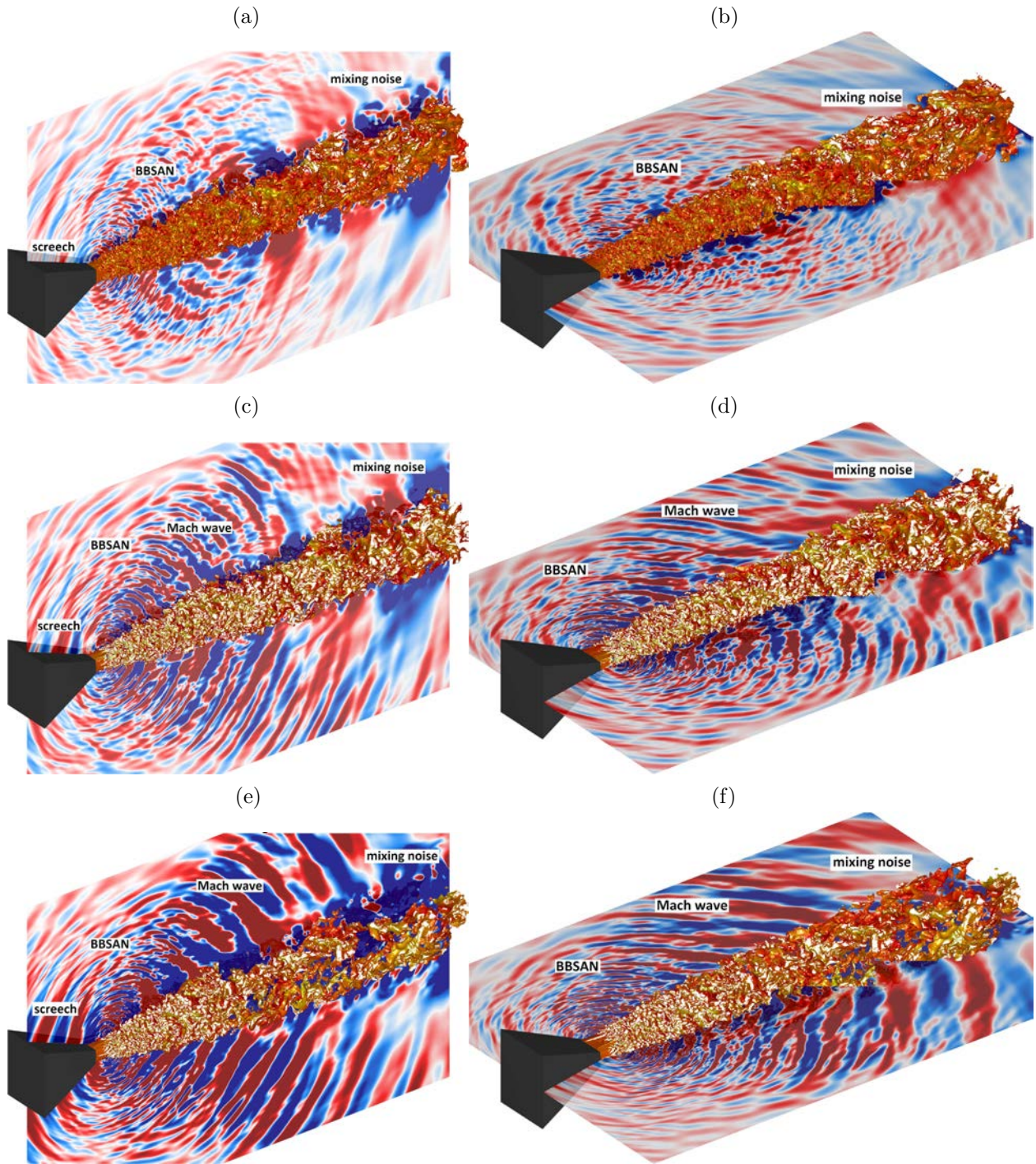


Figure 7. Isosurfaces of density colored by the Mach number for (a,b) Jet3TR1, (c,d) Jet3TR2 and (e,f) Jet3TR3. The pressure field along (a,c,e) the minor axis plane and (b,d,f) the major axis plane are also shown. The nozzle is in black.

propagates in the downstream direction and is associated to a low frequency. This acoustic contribution corresponds to the mixing noise, as observed by Bogey and Bailly [5], Sandham and Salgado [6] and Tam [7], for instance.

In Figure 7(c-f), for the higher temperature ratios investigated ( $TR = 2$  and  $TR = 3$ ), the temperature effect on the amplitude of the upstream propagating waves is observed. One can note that the amplitude of the upstream propagating waves is stronger along the minor axis plane than along the major axis plane. Moreover, these waves are visibly antisymmetric with respect to the jet axis. These two observations suggest that the screech mechanism in those jets is associated with a flapping motion of the jets along the minor axis. Moreover, it seems that the amplitude of the screech noise is increasing with the temperature. Secondly, when the temperature ratio increases, a new acoustic component arises in the sideline direction with long and straight acoustic waves organized along a clear direction. This acoustic contribution is linked to Mach wave radiation. This specific noise component appears when the convection velocity of the turbulent structures in the jet shear-layers becomes supersonic. This acoustic component has a marked directivity and a broadband spectrum. It has been studied experimentally [38] and numerically [39].

## V.B. Flow field statistics

The mean axial velocity fields obtained in the present LES for the four over-expanded jets are represented in Figure 8. Jet3TR1, Jet3TR2 and Jet3TR25 are compared to experimental PIV results in Figure 8(a,b,c,e,f,g). Despite of the unavoidable mismatch in the boundary conditions between the simulations and experiments there is an overall good agreement between the two sets of data. Moreover, as noted by Hsia *et al.* [40] for subsonic jets and by Zaman [41] for supersonic jets, a turbulent rectangular jet spreads faster along its minor axis than along its major axis. This evolution is visible in Figures 8 for the four over-expanded jets. In order to observe better this evolution, snapshots and mean fields of the density in the jet at different axial position are given for Jet3TR2 in Figure 9. The jet appears rectangular close to the nozzle exit, in Figure 9(a). Further downstream, the jet spreads mostly along the minor axis direction and an ellipse shape is visible in Figure 9(b), at  $z = 3h$ . The jet then evolves to a circular cross-section at  $z = 9h$ , and finally to an elliptical cross-section with its major axis aligned with the minor axis of the nozzle at  $z = 15h$ . In order to quantify this axis switching mechanism, the half velocity widths of the jets have been plotted along the minor axis and the major axis planes in Figure 10. It can be observed that the lower the temperature ratio of the jet, the higher the spreading of the jet is influenced by the shock-cell structure. Indeed, for Jet3TR1, the spreading of the jet follows the shock cell structure along both the major axis and the minor axis planes with oscillations amplitude of about  $0.1h$  whereas for Jet3TR3, the spreading of the jet appears not to follow the shock cell structure. Moreover, in Figure 10(b), the half velocity width of the jet along the major axis plane remains almost constant between  $z = 0$  and  $z = 15h$  whereas in Figure 10(a), the half velocity width of the jets along the minor axis plane increases from  $0.5h$  at  $z = 0$  to about  $1.4h$  at  $z = 15h$ . The switchover distance has been analysed in numerous studies in the past and this distance has been observed to depend on the internal nozzle geometry [42, 43], the properties of the flow at the nozzle exit [41] and the aspect ratio of the jet [42]. For the present jets, this distance is observed to increase with the temperature ratio, from  $7.5h$  for Jet3TR1 to  $11h$  for Jet3TR3.

Figure 8 shows that the length of the shock cells decreases in the downstream direction. This trend is due to the growth of the shear layer and to the dissipation of the shock-cell structure by the turbulence [44]. For supersonic rectangular jets, Tam [45] proposed a model to predict the length of the first shock cell. The model gives

$$L_{model} = 2(\mathcal{M}_j^2 - 1)^{1/2} \frac{h_j}{(1 + h_j^2/b_j^2)^{1/2}} \quad (5)$$

where  $h_j$  and  $b_j$  are the dimensions of the corresponding ideally expanded rectangular jet. For our aspect ratio 2 rectangular nozzle, their expressions [45] can be reduced to

$$\begin{aligned} \frac{h_j}{h} &= [(A_j/A_d) - 1] * 2/3 + 1 \\ \frac{b_j}{2h} &= [(A_j/A_d) - 1] * 1/3 + 1 \end{aligned}$$

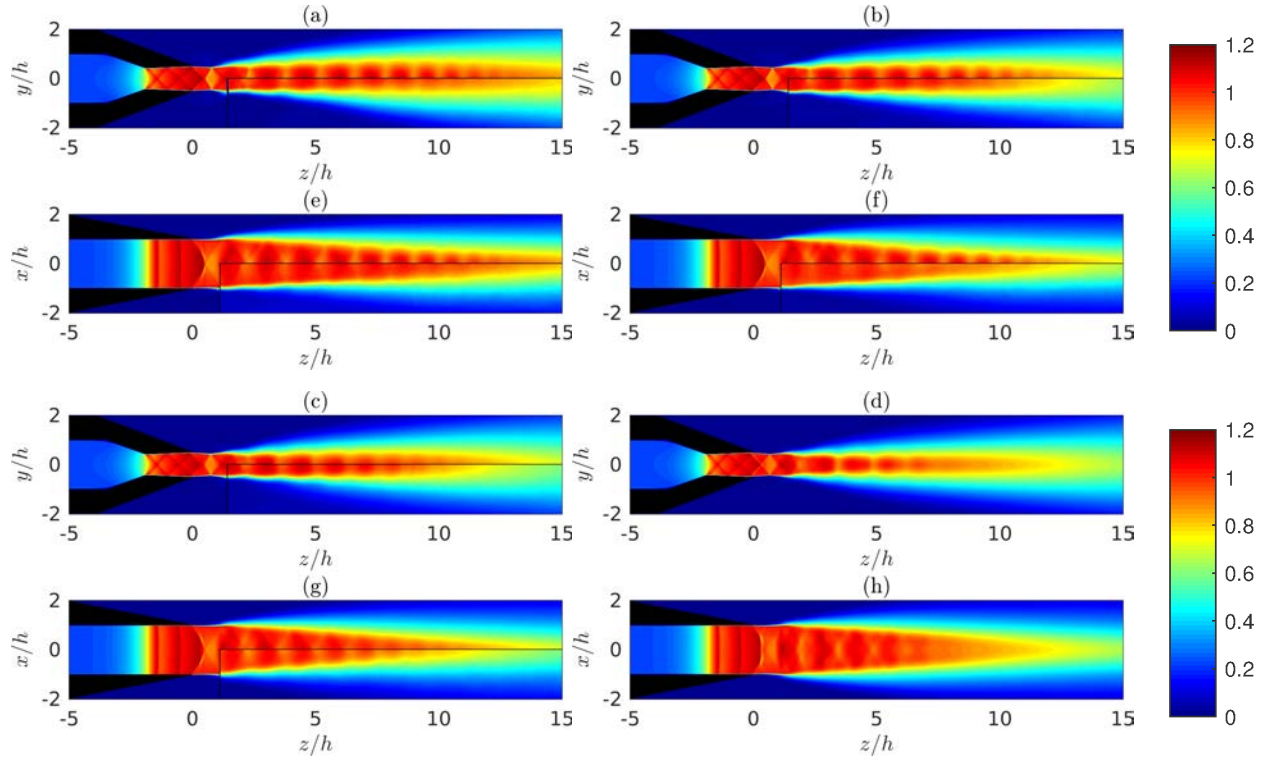


Figure 8. Mean axial velocity field  $\langle u_z \rangle / u_j$  for (a,e) Jet3TR1, (b,f) Jet3TR2, (c,g) Jet3TR25 and (d,h) Jet3TR3 along (a,b,c,d) the minor axis plane and (e,f,g,h) the major axis plane. The PIV results are added in the black rectangles. The nozzle is in black.

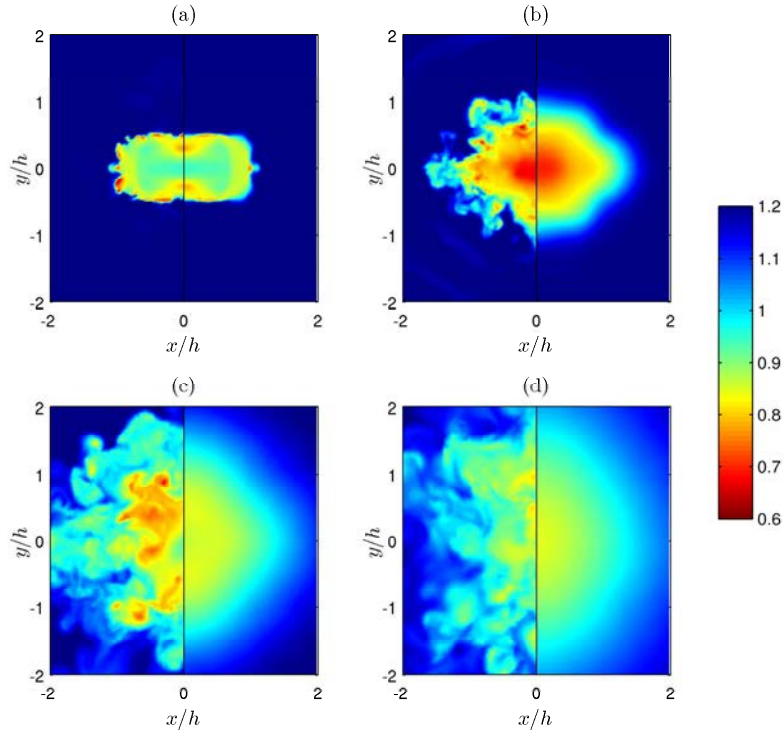


Figure 9. Snapshots (left) and mean fields (right) of the density in the  $(x, y)$  plane for Jet3TR2 at (a)  $z = h$ , (b)  $z = 3h$ , (c)  $z = 9h$  and (d)  $z = 15h$ .

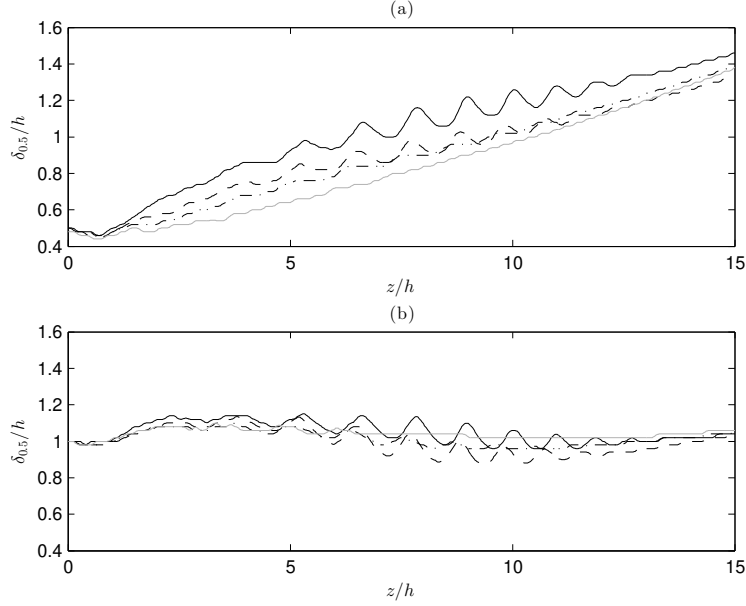


Figure 10. Half velocity width of the jets  $\delta_{0.5}/h$  along (a) the minor axis plane and (b) the major axis plane for — Jet3TR1, - - - Jet3TR2, - · - Jet3TR25, and - - - Jet3TR3.

where  $A_j$  is the nozzle exit area of the fully expanded equivalent jet and  $A_d = h * 2h$  is the nozzle exit area.  $A_j$  is given by

$$\left(\frac{A_j}{A_d}\right)^2 = \frac{\mathcal{M}_d^2}{\mathcal{M}_j^2} \left[ \left(1 + \frac{\gamma-1}{2} \mathcal{M}_j^2\right) / \left(1 + \frac{\gamma-1}{2} \mathcal{M}_d^2\right) \right]^{(\gamma+1)/(\gamma-1)}$$

where  $\mathcal{M}_d = 1.5$  is the design Mach number of the nozzle.

Equation (5) permits to find a value  $L_{model} = 1.57h$ . Values of  $L_s = 0.99L_{model}$ ,  $L_s = 0.97L_{model}$ ,  $L_s = 0.97L_{model}$  and  $L_s = 0.95L_{model}$  are found for the size of the first shock cell of Jet3TR1, Jet3TR2, Jet3TR25 and Jet3TR3, respectively. The size of the cell decreases by few percent with the jet temperature ratio but overall, the model gives a very good approximation for the length of the first shock cell. The normalized shock cell size  $L_s/L_{model}$  are reported in Figure 11 for all the visible cells in the mean fields of all investigated temperature ratios. The total number of shock cells visible decreases with the temperature ratio, from 10 for  $TR = 1$  to 4 for  $TR = 3$ . However, the variation of the shock-cell size appears to behave linearly for the four over-expanded jets. Such evolution was already observed by Harper-Bourne and Fisher [12] for round supersonic jets. They proposed a relation for the size of the  $n$ -th shock cell as follows:

$$L_n = L_s - (n - 1)\Delta L \quad (6)$$

where  $\Delta L$  is the variation of the cell size from one cell to another. For the present jets, a mean value of  $\Delta L/L_s = 5.5\%$  is obtained. For round underexpanded supersonic jets, André *et al.* [46] and Harper-Bourne and Fisher [12] found  $\Delta L/L_s = 3\%$  and  $\Delta L/L_s = 6\%$ , respectively. It is worth noting that the lower value found by André *et al.* [46] can be attributed to the presence of a secondary flow characterized by a Mach number of 0.05. To conclude, for our rectangular aspect ratio 2 jet, a linear evolution of the shock cell size similar to the one in round jets is observed.

Overall Sound Pressure Levels (OASPL) obtained along the minor and the major axis planes are presented for the four over-expanded jets in Figure 12. The OASPL is computed from the rms pressure fields. Several acoustic components are visible. The first acoustic component is visible in Figure 12(a,b,c,d) in the upstream direction along the minor axis plane. This component is linked to acoustic waves propagating in the upstream direction, permitting to close the aeroacoustic feedback loop leading to the screech noise. This acoustic component is only visible along the minor axis plane and its amplitude increases with the temperature ratio, confirming the observations made in Figure 7. Moreover, the cell structures obtained in the jets shear-layers in the amplitude fields of figure 12(c,d) for temperatures ratio of 2.5 and 3 are due to the presence of



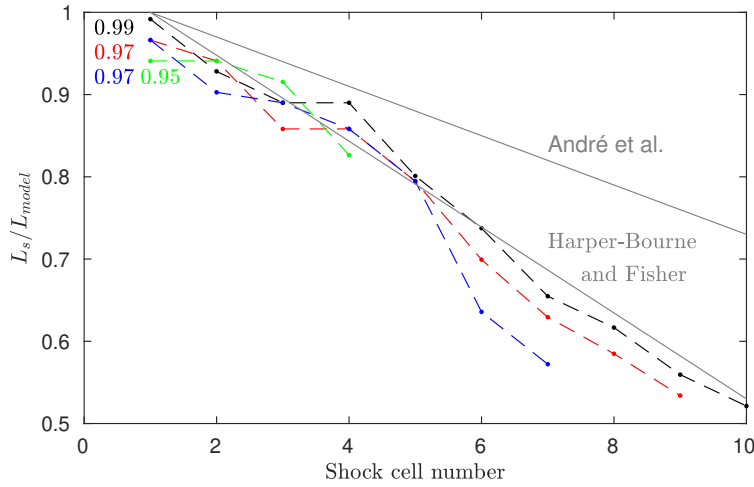


Figure 11. Normalized lengths of the shock cells obtained for —●— Jet3TR1, —●— Jet3TR2, —●— Jet3TR25, and —●— Jet3TR3.

hydrodynamic-acoustic standing waves created by the screech feedback loop. That is why they are present only along the minor axis plane. Such structures were previously observed by Panda *et al.* [47] for screeching supersonic jets and by Gojon *et al.* [34] and Bogey and Gojon [33] for ideally expanded impinging jets. The second acoustic component visible is linked to the Mach wave radiation, whose intensity increases with the temperature ratio. Moreover, it can be seen that this component is organized in an axisymmetric manner for Jet3TR2 in Figure 12(b,f) but in a asymmetric manner for Jet3TR25 and Jet3TR3 in Figure 12(c,d,g,h) with much stronger Mach wave radiation along the minor axis plane compared to the major axis plane. The strong flapping motion of the jet along the minor axis due to the screech feedback mechanism seems to lead to this asymmetric organization of the Mach wave radiation.

In order to assess the presence of the Mach wave radiation in the hot cases, the convection velocity of turbulent structures in the jet shear layers is computed. It is calculated in the jet shear layers, where the turbulence kinetic energy is maximum, from cross-correlations of axial velocity between 70 neighbouring points equidistantly spaced at  $0.25h$  from each other. In practice, for a reference point, cross correlations with its two neighbours are computed and the time lag between the reference point and its neighbours is fitted by a straight line. The slope of the line gives then the local convection velocity. For the over-expanded jets, the normalized convection velocity and the convective Mach number along the jet shear layer in the minor axis plane are represented in Figure 13. For all the jets, the convection velocity is not constant but varies according to the shock cell structure, as already observed for round jets experimentally [9] and numerically [48]. The mean values of the convection velocity and of the convective Mach number between  $z = 1$  and  $z = 15$  along the minor axis plane are reported in Table 2. Overall, the mean normalized convection velocity  $\langle u_c \rangle$  of the turbulent structures decreases with the increase of the temperature ratio, from  $0.80u_j$  to  $0.64u_j$ . The same observation has been made numerically in a recent study by Liu *et al.* [49] Indeed, for round supersonic underexpanded jets, they found the convection velocity to decrease from  $0.68u_j$  for a temperature ratio of 1 to  $0.56u_j$  for a temperature ratio of 7. In Figure 13(b), the convective Mach number remains below 1 for Jet3TR1, resulting in the absence of Mach waves in Figure 7(a,b). For Jet3TR2, Jet3TR25 and Jet3TR3, a convective Mach number of about  $\mathcal{M}_c = 1.25$  is found. This supersonic Mach number yields the creation of the Mach waves observed in Figure 7(c-f).

	$u_j$ (m.s <sup>-1</sup> )	$\langle u_c/u_j \rangle$	$\mathcal{M}_c = \langle u_c/a_0 \rangle$
Jet3TR1	398	0.80	0.94
Jet3TR2	563	0.73	1.21
Jet3TR25	629	0.68	1.25
Jet3TR3	689	0.64	1.29

Table 2. Convection velocity along the minor axis plane: ideally expanded velocity  $u_j$ , mean convection velocity  $\langle u_c/u_j \rangle$  and mean convective Mach number  $\mathcal{M}_c = \langle u_c/a_0 \rangle$ .



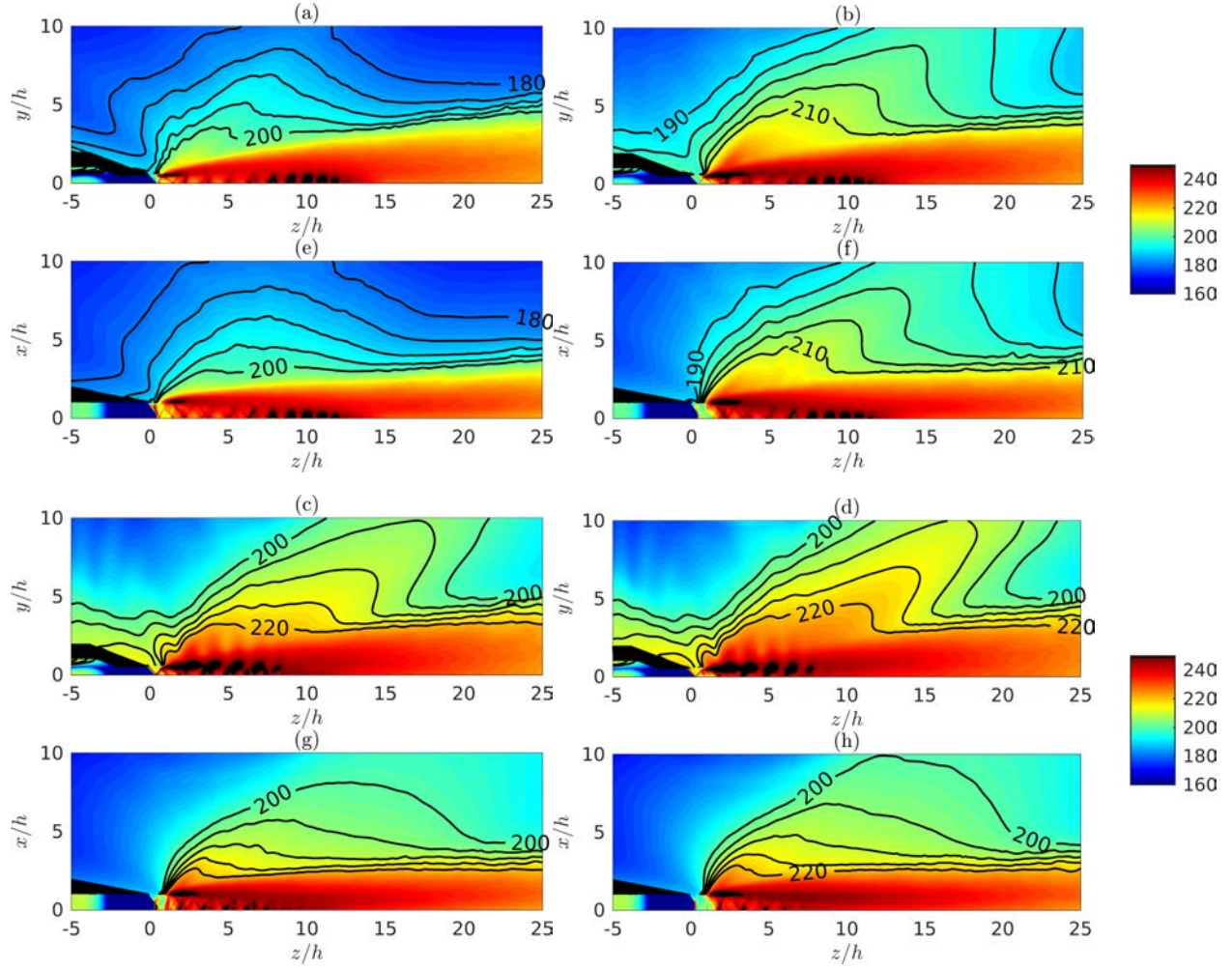


Figure 12. Overall Sound Pressure Levels for (a,e) Jet3TR1, (b,f) Jet3TR2, (c,g) Jet3TR25 and (d,h) Jet3TR3 along (a,b,c,d) the minor axis plane and (e,f,g,h) the major axis plane. The nozzle is in black.

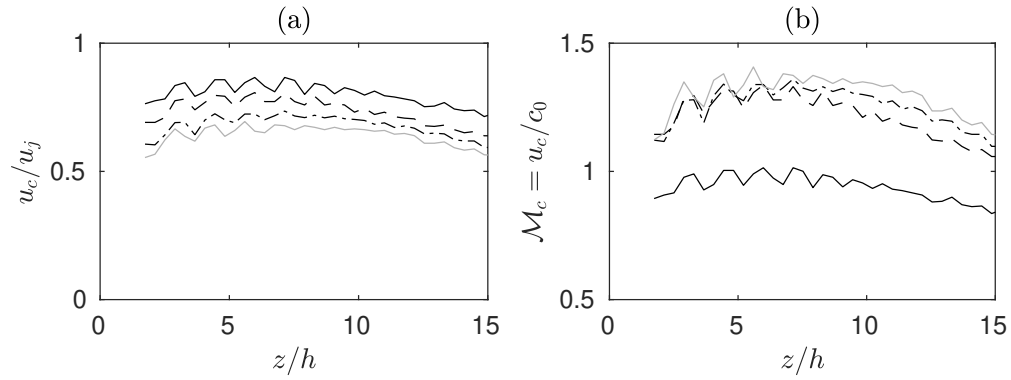


Figure 13. (a) Convection velocity and (b) convective Mach number  $\mathcal{M}_c$  of the turbulent structures along the jet shear-layer in the minor axis plane as a function of the axial position for — Jet3TR1, — — — Jet3TR2, — · — Jet3TR25, and — Jet3TR3.

## VI. Acoustic results

### VI.A. Near-field acoustics

The pressure spectra obtained in the vicinity of the nozzle at  $(x, y, z) = (0, -2h, -2h)$  are depicted in Figure 14 as a function of the Strouhal number  $St = fD_{eq}/u_j$ . There is a change in the dominant frequency as the jet's temperature changes, with dimensionless frequencies ranging between  $St = 0.29$  and  $St = 0.36$ . Those frequencies, visible in the upstream direction in the vicinity of the jet, correspond to the screech components [14, 16, 17, 35, 36]. A secondary peak whose frequency is ranging between  $St = 0.16$  and  $St = 0.21$  and the first harmonic of the screech frequency can also be seen. This noise component could be associated to the mixing noise. Indeed, even if this component is dominant in the downstream direction, André [9] observed such component at angles of 30 degrees with respect to the upstream direction.

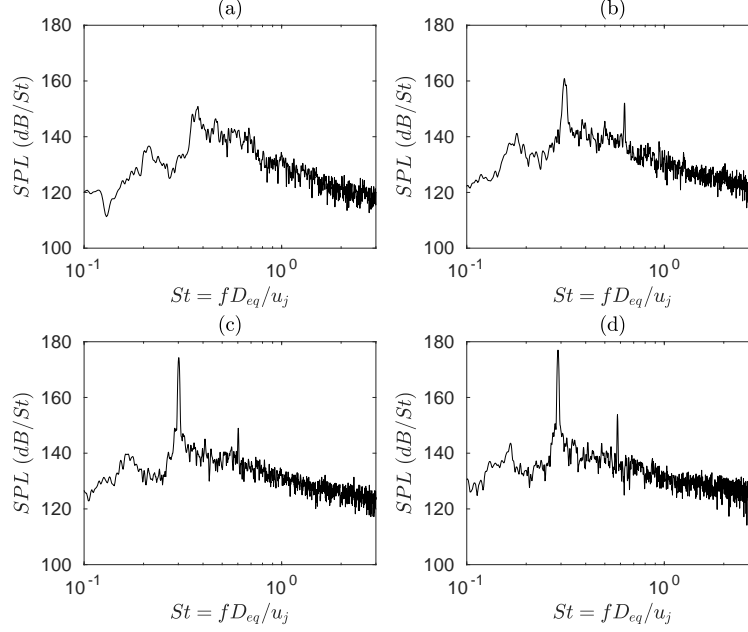


Figure 14. Pressure spectra at  $(x, y, z) = (0, -2h, -2h)$  as a function of the Strouhal number for (a) Jet3TR1, (b) Jet3TR2, (c) Jet3TR25 and (d) Jet3TR3.

For the four over-expanded jets, the amplitude and the frequency of the low frequency and screech components are given in Table 3. The screech frequencies found experimentally [20] are also reported. For the low frequency component, its Strouhal number is decreasing with the temperature ratio from  $St = 0.21$  for Jet3TR1 to  $St = 0.16$  for Jet3TR3, with an amplitude globally increasing from 136dB/St for Jet3TR1 to 144dB/St for Jet3TR3. For the screech component, the Strouhal number is decreasing from  $St = 0.37$  for Jet3TR1 to  $St = 0.29$  for Jet3TR3 and the amplitude is increasing from 151dB/St for Jet3TR1 to 177dB/St for Jet3TR3. The Strouhal numbers are in excellent agreement with the experimental results from University of Cincinnati [20]. Please note that those frequencies have been reported using a far-field microphone array organized along the minor axis plane. However, Mora *et al.* [20] observed an overall decrease of the amplitude of the screech component with an increase of the temperature ratio, in contradiction with the present increase. For a rectangular jet, Tam [45] proposed a model to predict the screech frequency. In the present scenario (2:1 AR rectangular jet), the model gives:

$$St_{Tam} = \frac{\frac{D_{eq}u_c/u_j}{2h(1+u_c/a_0)(\mathcal{M}_j^2-1)^{1/2}}((h_j/b_j)^2+1)^{1/2}}{\left(\left(\frac{1+\frac{\gamma-1}{2}\mathcal{M}_j^2}{1+\frac{\gamma-1}{2}\mathcal{M}_d^2}\right)^{(\gamma+1)/(2(\gamma-1))} \frac{\mathcal{M}_d}{\mathcal{M}_j} - 1\right) \frac{2}{3} + 1} \quad (7)$$

The values found by evaluating equation (7) using the mean convection velocity and mean convective Mach number from Table 2 are reported in Table 3. For Jet3TR2, Jet3TR25, and Jet3TR3, a very good

agreement is found between the simulation results, the experimental results, and the value found using equation (7). For Jet3TR1, equation (7) yields to an overestimation of about 10% of the screech frequency. Overall, the decrease of the frequency of the screech component with the temperature ratio is obtained using equation (7).

	$St_{low}$	$dB_{low}$	$St_{screech}$	$dB_{screech}$	$St_{screech}$ exp.	$St_{screech}$ Tam
Jet3TR1	0.21	136	0.37	151	0.37	0.41
Jet3TR2	0.18	141	0.31	160	0.31	0.33
Jet3TR25	0.17	140	0.30	174	—	0.30
Jet3TR3	0.16	144	0.29	177	0.28	0.28

**Table 3.** Frequencies  $St_{low}$  and  $St_{screech}$  and amplitudes  $dB_{low}$  and  $dB_{screech}$  of the two tone frequencies emerging in Figure 14 for each jet; screech frequency  $St_{screech}$  exp. found in the experimental study [20]; screech frequency  $St_{screech}$  Tam found using the model of Tam [45].

## VI.B. Far-field acoustics

The Ffowcs Williams-Hawkings (FW-H) surface used to compute the far-field acoustics is represented in Figure 15 along the minor axis plane for the case Jet3TR2. It is an ellipsoid englobing the nozzle and the jet flow. It is placed at the end of the first acoustic zone in the structured mesh, corresponding to a Strouhal number resolved of  $St \sim 6$ . The surface consists of about 1 million nodes and the flow variables are stored at a sampling frequency corresponding to  $St \sim 10$ . Please note that the surface is placed quite far from the jet compared to other studies [30, 50, 51]. It was too expensive in terms of storage to use the method with several outflow disks of Shur *et al.* [50], used for example by Brès *et al.* [51] and in the case of an open surface, a "loose" FW-H surface is then preferable [50]. Indeed, this surface located quite far from the jet permits to avoid the creation of "pseudo-sound" [52]. This unphysical sound results from the convection through the surface of slow turbulent structures that are not cancelled because of the absence of the outflow disk.

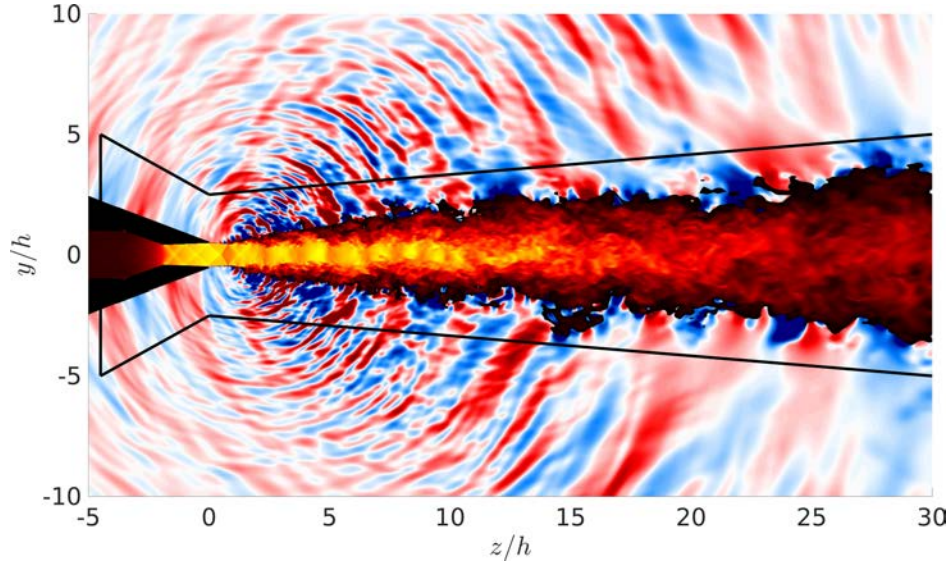


**Figure 15.** Representation of the contour of the FW-H surface in black over a 2-D snapshot along the minor axis plane representing the Mach number in the jet and the fluctuating pressure around for Jet3TR2. The nozzle is in black.

The FW-H surface is used to compute the fluctuating pressure in the far-field at a distance of  $40D_{eq}$  along the minor axis plane, using  $(x, y, z) = (0, 0, 0)$  as reference point. The FW-H equations for a stationary permeable integral surface are used, they can be found in details in Yao *et al.* [53] The OASPL directivity in the far-field of the jet on the minor axis plane is shown for the four over-expanded jets in Figure 16 and compared to the experimental results for Jet3TR1, Jet3TR2 and Jet3TR3. Overall, a good agreement is reached.

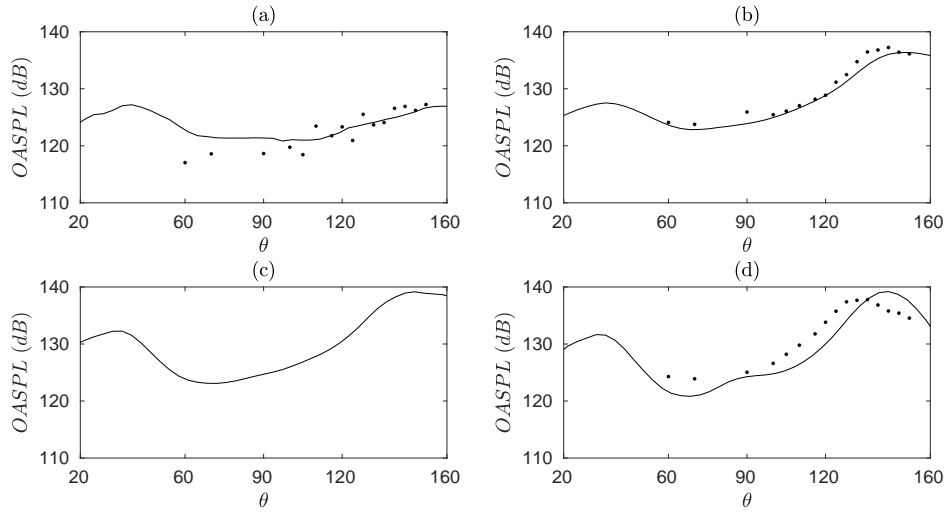


Figure 16. OASPL obtained on the circle of radius  $R = 40D_{eq}$  in the minor axis plane as functions of the angle  $\theta$  with respect to the upstream direction for (a) Jet3TR1, (b) Jet3TR2, (c) Jet3TR25 and (d) Jet3TR3;  $\bullet$  experimental results and  $—$  current results (LES & FW-H).

The acoustic spectra in the far-field are shown in Figure 17 as a function of the Strouhal number and the directivity angle, with 20 degrees being the most upstream location and 160 degrees angle corresponding to the most downstream side angle. Several acoustic components typical of non-ideally expanded supersonic jets can be seen in Figure 17. In the upstream direction, for  $\theta < 60$  degrees, the screech tone frequencies dominate, as already pointed out in the pressure spectra of Figure 14. In the downstream direction, for  $\theta > 140$  degrees, the mixing noise generated by large scale turbulent structures appears around a Strouhal number of 0.25. The directivity and frequency of this acoustic component are in good agreement with the numerical results of Berland *et al.* [3] for a planar supersonic jet with  $\mathcal{M}_j = 1.55$ . A third acoustic component is visible for  $60 < \theta < 160$  degrees. Its central frequency is varying with the angle of observation. This component is associated with broadband shock-associated noise, as observed in experimental [9–11] and numerical [3, 37] studies. A mechanism was proposed by Harper-Bourne and Fisher [12] for this acoustic component. In this mechanism, the broadband shock-associated noise is generated by the interactions between the turbulent structures propagating downstream in the jet shear layers and the shocks of the shock cell structure. Each interaction is considered as an acoustic source. The directivity of constructive interference is then determined. This model yields a central frequency given by:

$$f_{shock} = \frac{Nu_c}{L_{sh}(1 + \mathcal{M}_c \cos(\theta))} \quad (8)$$

where  $N$  is the mode number,  $L_{sh}$  is a length scale related to the shock cell size, and  $\mathcal{M}_c$  is the convective Mach number. As the cell length varies with the axial direction, it is difficult to choose a value of  $L_{sh}$ . A value of  $L_{sh} = 0.8L_{model}$  is used for our study. The corresponding central frequency of the broadband shock-associated noise is represented with dashed line in Figure 17 for  $N = 1$  and using the values in Table 2 for  $u_c$  and  $\mathcal{M}_c$ . A good overall agreement is found. It is worth noting that at angles around  $\theta = 90$  degrees, for Jet3TR2, Jet3TR25 and Jet3TR3, the first harmonics of the screech component coincide with the BBSAN component and becomes dominant. The same observation has been made by the experimental study [20]. One can finally note that in the upstream direction, the relation (8) tends to the values of  $St = 0.50$ ,  $St = 0.48$ ,  $St = 0.45$  and  $St = 0.44$  for Jet3TR1, Jet3TR2, Jet3TR25 and Jet3TR3, respectively. Those tones are visible in the spectra of Figure 14, between the screech tones and their harmonics. Finally, for Jet3TR2, Jet3TR25 and Jet3TR3, a fourth acoustic component is visible at an angle of  $\theta = 140$  degrees. This broadband component corresponds to the Mach wave radiation. Its directivity is given by the following model of Oertel [13]:

$$\theta = 180 - \arccos\left(\frac{1}{\mathcal{M}_c}\right) \quad (9)$$

where  $\phi$  is the angle with respect with the jet axis and  $\mathcal{M}_c$  is the convective Mach number.

Using a convective Mach number of  $\mathcal{M}_c = 1.25$ , relation (9) gives an angle of  $\theta = 143$  degrees. This angle is also in agreement with the peak values visible in Figure 16(b-d) for Jet3TR2, Jet3TR25 and Jet3TR3.

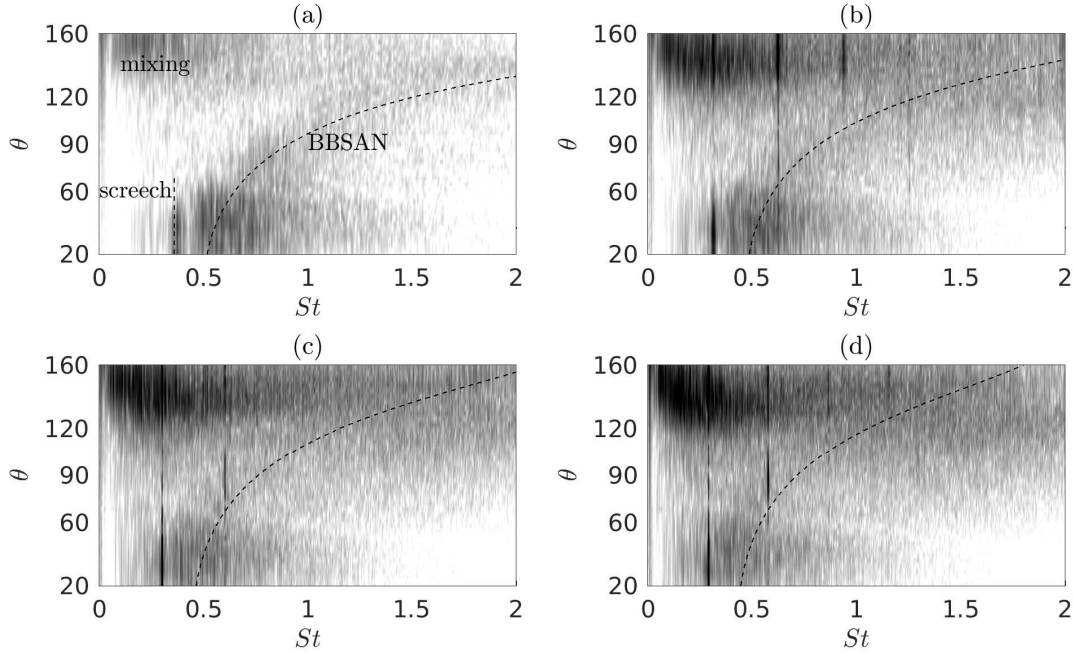


**Figure 17.** Far-field SPL as predicted based on the FW-H approach  $R = 40D_{eq}$  as a function of the Strouhal number and of the angle  $\theta$  with respect to the upstream direction; data in the minor axis plane of the jet for (a) Jet3TR1, (b) Jet3TR2, (c) Jet3TR25 and (d) Jet3TR3. The colour scale ranges from 110 and 140 dB/St.

Acoustic spectra at three different angles are given in Figure 18 to increase readability and to compare to experiments for Jet3TR1, Jet3TR2 and Jet3TR3. For the broadband noise, a good agreement is reached. More specifically, for the broadband shock associated noise, the characteristic hump is recovered, and its frequency is in agreement with experimental results. For the screech, as already pointed out in a previous section, the frequency is well reproduced but the amplitude is not. More precisely, the amplitude of the screech frequency increases with the temperature in the simulation whereas it decreases in the experiments.

## VII. Fourier decomposition of the pressure field

For each jet, the pressure field have been recorded every 100 time step. In order to be able to store and to analyse such a large volume of data, a subset of 6 million points is considered. A Fourier transform is then applied to all points, permitting to plot, for a given frequency, its amplitude and phase. For the four over-expanded jets, the screech frequency is considered. Figure 19 represents isosurfaces of the amplitude in the jet and phase along the major and the minor planes.

For Jet3TR1, in figure 19(a), a structure with alternating positive and negative values is found. The structure is organized along the diagonal of the jet, indicating that the jet is flapping along diagonal of the jet at the screech frequency. This result is consistent with the phase. Indeed, 180 degrees phase shifts are visible along the minor and the major axis planes. This result is also consistent with the almost axisymmetric radiation of the jet observed in Figure 12 and with an experimental study by Raman [54] for a cold rectangular supersonic jet of aspect ratio 4.76. He observed a dominant screech mechanism organized with 180 degrees phase shifts along the minor and the major axis planes in the region near the nozzle exit for an ideally expanded Mach number  $\mathcal{M}_j$  between 1.263 and 1.41. For Jet3TR2, in figure 19(b), two types of structures are found in the jet. First, near the jet exit, antisymmetric structures organized along the minor axis plane are observed. Then, further downstream, structures organized along the diagonal of the jet can be seen. These latter structures are similar to those observed for Jet3TR1, in figure 19(a). In the phase contours, a 180 degrees phase shift is observed along the minor axis plane and a small phase shift of about 90 degrees can be noted along the major axis plane. Thus, in this case, the jet undergoes a complex motion

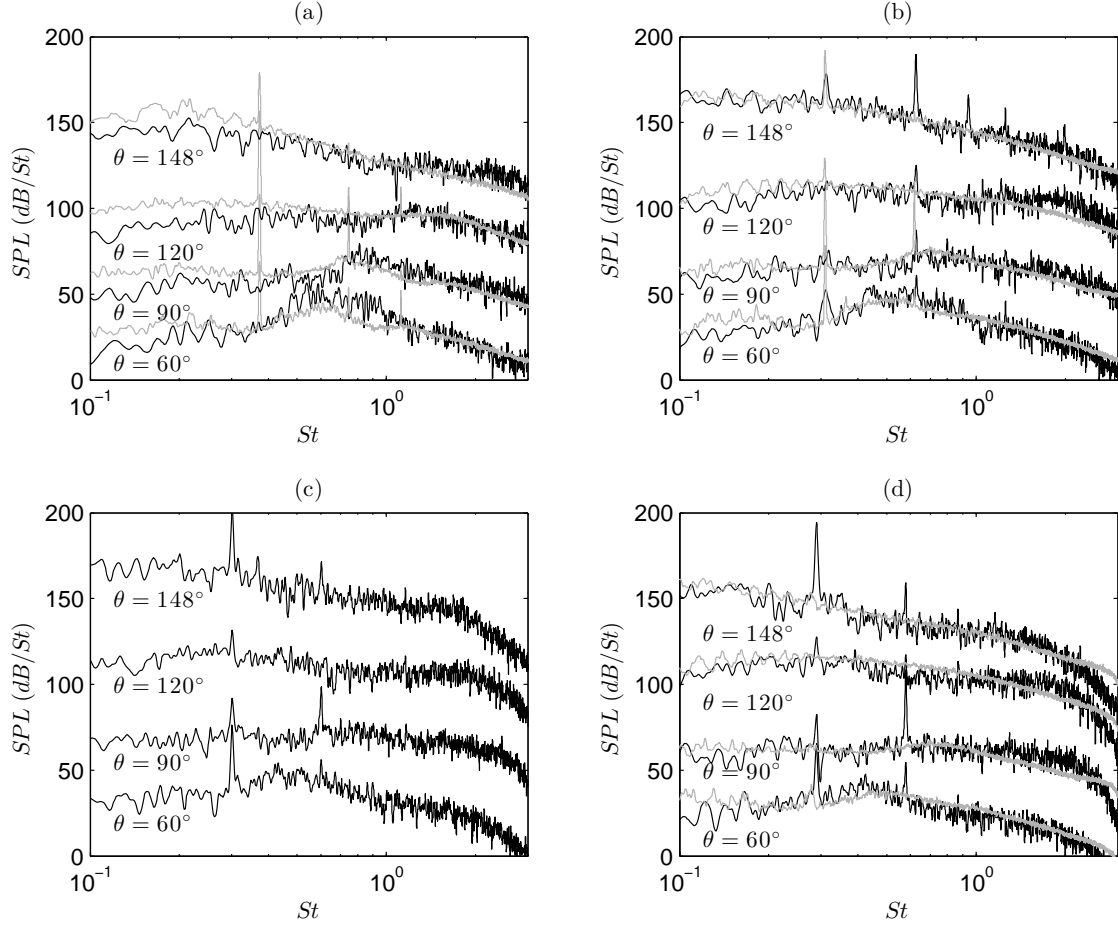


Figure 18. Far-field SPL at  $R = 40D_{eq}$  as a function of the Strouhal number; data in the minor axis plane of the jet for (a) Jet3TR1, (b) Jet3TR2, (c) Jet3TR25 and (d) Jet3TR3; — current results (LES & FW-H) and — experimental results. The scale is arbitrary and a 30 dB offset is used between each angle.



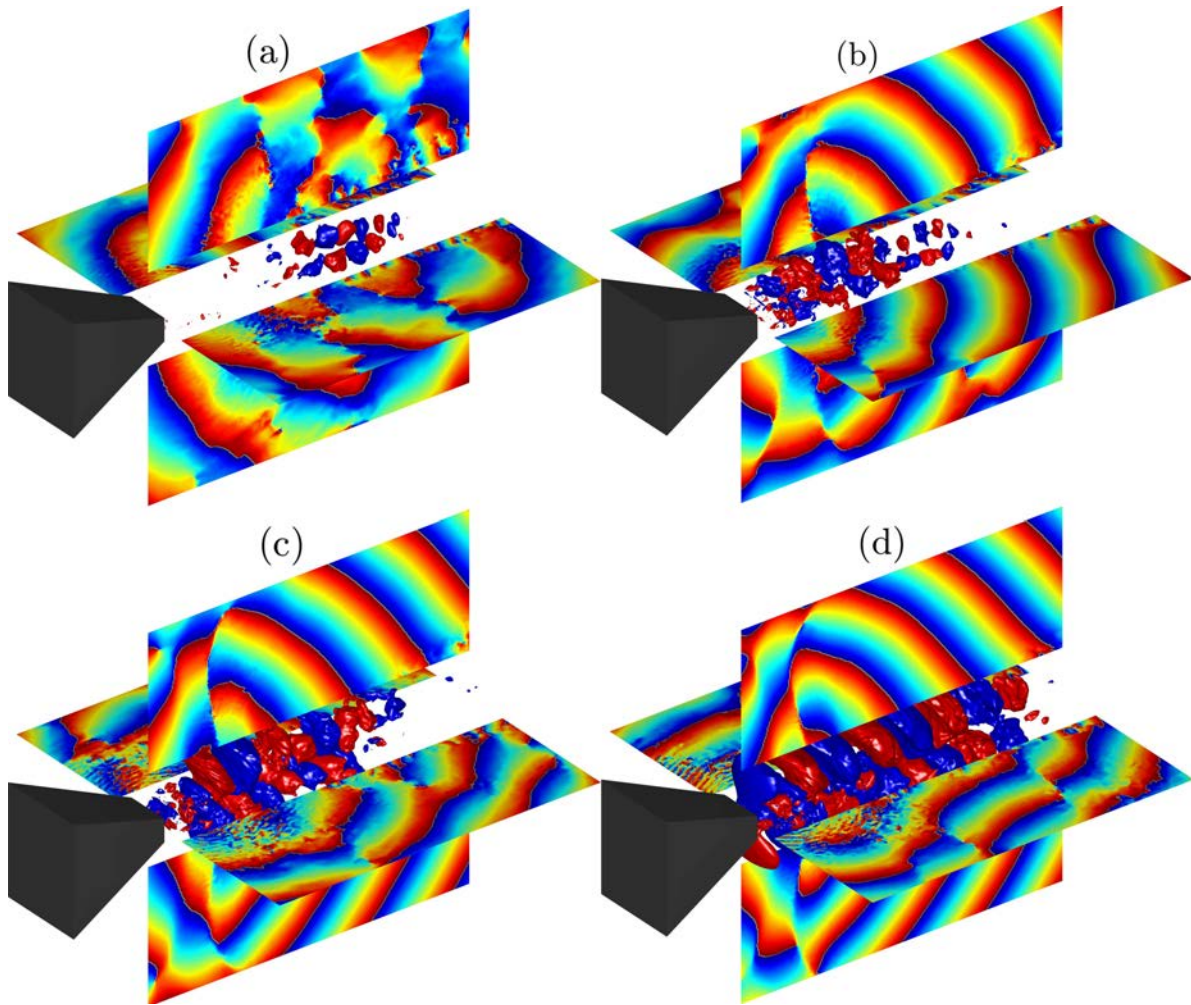


Figure 19. Isosurfaces of positive (red) and negative (blue) values of the amplitude in the jet and phase along the major and the minor planes for (a) Jet3TR1 ( $St = 0.36$ ), (b) Jet3TR2 ( $St = 0.31$ ), (c) Jet3TR25 ( $St = 0.30$ ) and (a) Jet3TR3 ( $St = 0.29$ ). The colour scale ranges from  $-\pi$  to  $\pi$  for the phase fields.

at the screech frequency consisting mainly of a flapping component along the minor axis plane but also of a flapping motion along the diagonal of the jet. For Jet3TR25 and Jet3TR3, in figure 19(c,d), structures with alternating positive and negative values organized along the minor axis plane are visible. In the phase fields, phase shifts can be seen along the minor axis plane but not along the major axis plane. This implies that the jets undergo a purely flapping motion along the minor axis plane at the screech frequencies. The jump in screech frequency between Jet3TR1 and the three other cases could be related to the jump observed experimentally from mode II (antisymmetric along the major axis plane) to mode I (symmetric along the major axis plane) as noted in Raman [54]. Finally, as already observed in Figure 12, the cell structures observed in the amplitude contours of figure 19 are due to the formation of flow-acoustic standing waves.

## VIII. Wave analysis using a vortex sheet model of the jet

In the present paper, as in the work by Shen and Tam [55] and Gojon *et al.* [18] for round screeching jets, it is assumed that the feedback loop causing screech noise in non-ideally expanded jets is closed by acoustic waves belonging to the family of the upstream-propagating acoustic wave modes of the equivalent ideally expanded jet. The dispersion relations of these instability waves can be approximated by using a vortex sheet model of the jets as in Tam and Norum [56]. They started from the linearized governing equations for a compressible inviscid fluid flow. Remarking that the acoustic waves are neutral for a vortex-sheet model, i.e. that they have both real wavenumber  $k$  and angular frequency  $\omega$ , Tam and Norum [56] obtained for an ideally expanded rectangular jet the following relations:

$$\frac{[(\omega - u_j k)^2 / a_j^2 - k^2]^{1/2} \rho_0 \omega^2}{(k^2 - \omega^2 / a_0^2)^{1/2} \rho_j (\omega - u_j k)^2} - 1 / \tan \left\{ \left[ \frac{(\omega - u_j k)^2}{a_j^2} - k^2 \right]^{1/2} h_j / 2 \right\} = 0 \quad (10)$$

for symmetric modes, and

$$\frac{[(\omega - u_j k)^2 / a_j^2 - k^2]^{1/2} \rho_0 \omega^2}{(k^2 - \omega^2 / a_0^2)^{1/2} \rho_j (\omega - u_j k)^2} + \tan \left\{ \left[ \frac{(\omega - u_j k)^2}{a_j^2} - k^2 \right]^{1/2} h_j / 2 \right\} = 0 \quad (11)$$

for antisymmetric modes. The jet is characterized by the jet diameter  $D_j$ , exit velocity  $u_j$  and Mach number  $\mathcal{M}_j$ . In Eqs. (10) and (11),  $a_0$  and  $a_j$  are the sound speeds in the ambient medium and in the jet,  $\rho_0$  is the density in the ambient medium,  $k$  is the wave number and  $\omega$  is the angular frequency of the wave.

As it can be seen in the dispersion relations (10) and (11), only the height  $h_j$  of the ideally-expanded associated nozzle influences this 2-D model. Thus, the Strouhal number  $St_{hj} = fh_j / u_j = St \times h_j / D_{eq}$  is defined for this section.

For the seven considered jets, the screech Strouhal numbers  $St_{screech}$  and its corresponding Strouhal number  $St_{hj}$  are given in Table 4. The experimental screech Strouhal numbers are also displayed. For the seven operating conditions, the screech frequency found in the simulation match the one observed in the experiment, suggesting that the feedback loop responsible for the screech noise is correctly reproduced and that our numerical setup is capable of predicting the screech frequency for over- and under-expanded rectangular jets.

	$St_{screech}$	$St_{screech exp}$	$St_{hj}$
Jet3TR1	0.36	0.37	0.215
Jet3TR2	0.31	0.31	0.185
Jet3TR25	0.30	—	0.18
Jet3TR3	0.29	0.28	0.175
Jet4TR1	0.24	0.25	0.155
Jet4TR2	0.18	0.17	0.115
Jet4TR3	0.12	0.11	0.077

**Table 4.** Screech Strouhal numbers  $St = fD_{eq}/u_j$  and  $St_{hj} = fh_j/u_j$ .

The solutions of the relation dispersions (10) and (11) calculated for the present jets with a nozzle pressure ratio of 3 are represented in Figure 20 as functions of the Strouhal number  $St_{hj} = fh_j/u_j$  and



the wave number. Four symmetric neutral acoustic wave modes referred to as  $S1$ ,  $S2$ ,  $S3$  and  $S4$  appear in figure 20(a). In the same way, four antisymmetric modes denoted by  $A1$ ,  $A2$ ,  $A3$  and  $A4$  are found in figure 20(b).

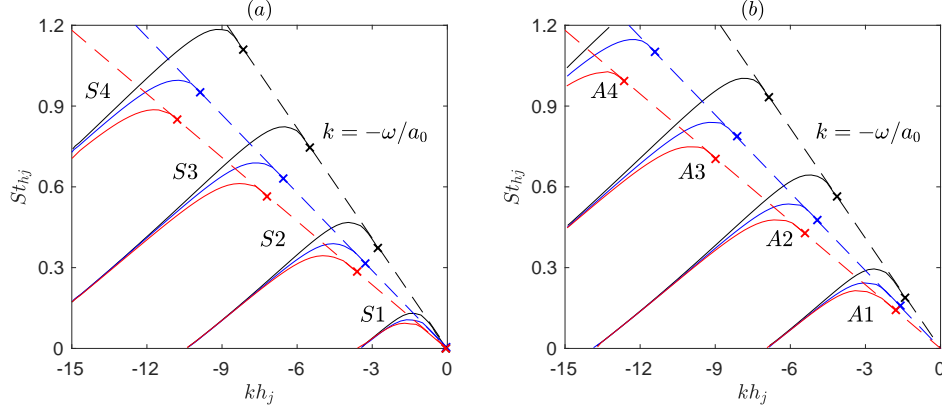


**Figure 20.** Dispersion relations for (a) the symmetric and (b) the antisymmetric neutral acoustic wave modes for an ideally expanded planar jet with  $\mathcal{M}_j = 1.36$ ,  $\times$  lower limits of the modes,  $---$   $k = -\omega/a_0$ . The results for TR1, TR2 and TR3 are respectively in black, blue and red.

According to Tam and Hu [57], upstream propagating acoustic waves are present in high-speed jets. They are confined in the jets when the jets are subsonic, but lie outside when the jets are supersonic. Such waves are found in Figure 20 on the right-hand side of each mode where  $dSt/dk < 0$ , leading to a negative group velocity  $d\omega/dk$ . Allowable frequency ranges can thus be determined for the different modes. Their upper limits, which correspond to the maximum Strouhal numbers reached for the modes when  $dSt/dk = 0$ , are obtained from the figure. Their lower limits are calculated, since they are necessarily associated with acoustic waves propagating with a group velocity of  $-a_0$ , and located on the dashed line of figure 20 defined by

$$k = -\frac{\omega}{a_0} \quad (12)$$

For  $k = -\omega/a_0$ , the first terms in equations (10) and (11), and consequently the second terms, tend to infinity. The argument of the tangent function needs to be equal to

$$\left[ \frac{(\omega - u_j k)^2}{a_j^2} - k^2 \right]^{1/2} \frac{h}{2} = \frac{n-1}{\pi} \quad (13)$$

for equations (10) and

$$\left[ \frac{(\omega - u_j k)^2}{a_j^2} - k^2 \right]^{1/2} \frac{h}{2} = \frac{n-1/2}{\pi} \quad (14)$$

for equations (11). This yields to the following Strouhal numbers for the lower limits of the allowable frequency ranges

$$St = \frac{n-1}{u_j \left( (1 + u_j/a_0)^2/a_j^2 - 1/a_0^2 \right)^{1/2}} \quad (15)$$

for the symmetric modes and

$$St = \frac{n-1/2}{u_j \left( (1 + u_j/a_0)^2/a_j^2 - 1/a_0^2 \right)^{1/2}} \quad (16)$$

for the antisymmetric modes, where  $n$  is the mode number. The values calculated for the present jet are depicted in Figure 20.

The allowable frequency ranges determined for the two first symmetric and antisymmetric upstream propagating wave modes are represented in figure 21 as a function of the ideally expanded Mach number  $\mathcal{M}_j$  for temperature ratios of 1 and 2. Screech frequencies measured by Panda *et al.* [47], Raman [54] and Alkislar *et al.* [58] for cold rectangular supersonic screeching jets are also shown in Figure 21(a). In Figure 21(b), experimental results of Raman and Rice [19] for a rectangular screeching jet with a temperature ratio of

2 are added. The screech frequencies obtained for the four jets at temperature ratios of 1 and 2 are also plotted in the figure. All the screech frequencies lie in the allowable range for the first antisymmetric mode or just below. In a similar way as in round screeching jets [18, 55], planar impinging jets [34] and round impinging jets [33], the present wave analysis thus appears to predict the nature of the jet oscillation mode at the tonal frequency. The disagreements observed, with screech tone frequencies located slightly below the allowable frequency range for the mode A1 may be due to the use of a vortex-sheet jet model instead of a jet with a mixing layer of finite thickness. Indeed, as observed by [59], this model increases the lower limits of the mode for subsonic jets and a similar behaviour can be expected for supersonic jets.

	Nozzle	Aspect ratio	design Mach number	Total temperature
Panda <i>et al.</i> [47]	convergent nozzle	5	1	294K
Raman [54]	convergent-divergent nozzle	4.75	1.4	300K
Alkislar <i>et al.</i> [58]	convergent-divergent nozzle	4	1.44	336K
Raman and Rice [19]	convergent nozzle	9.63	1	545K

Table 5. Characteristics of different experiments on rectangular screeching jets.

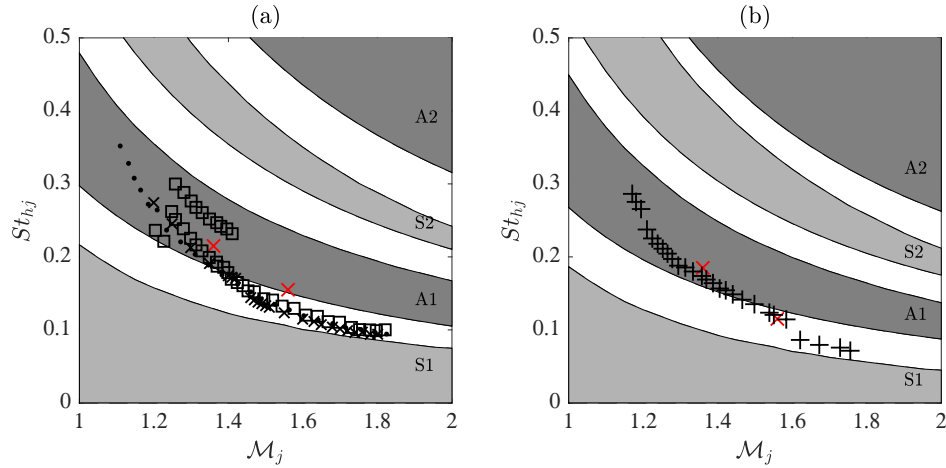


Figure 21. Representation of the allowable frequency ranges for upstream-propagating neutral acoustic wave modes in a planar jet with (a) a temperature ratio of 1 and (b) a temperature ratio of 2 as a function of the ideally-expanded Mach number; the light-grey and the dark-grey bands correspond to symmetric and antisymmetric oscillation modes of the jet; Panda *et al.* [47] •, Raman [54] □, Alkislar *et al.* [58] ×, Raman and Rice [19] + and present LES ×.

In order to detect upstream-propagating waves in the present jet, following previous work on ideally expanded impinging jets [33], on subsonic free jet [60], and on round screeching jets [18], a space-time Fourier transform has been applied to the pressure fluctuations at different transverse positions between  $z = 0$  and  $z = 10h$ . The frequency-wavenumber spectra obtained at  $y = 0.1h$  for the symmetrical ( $n = 0$ ) and antisymmetrical ( $n = 1$ ) modes at  $y = 0.1h$ ,  $y = 0.25h$  and  $y = 0.5h$  are represented in Figures 22, 23, 24 and 25 for the jets with temperatures ratios 2 and 3 as functions of the Strouhal number  $St_{hj} = fh_j/u_j$  and of the normalized axial wavenumber  $kh_j$ . The dispersion relations of the neutral acoustic wave modes of the equivalent ideally expanded jet are also displayed.

For the four jets, at  $y = 0.1h$  significant levels are found slightly above the theoretical curves associated with the modes S1 and A1. Moreover, for the symmetric mode, significant amplitudes are found in Figures 22, 23, 24 and 25(a,b,d) slightly above the theoretical curves associated with the mode S1. The discrepancies with respect to the model may be due to shock oscillations in the simulated jets, and to the use of an infinitely thin shear layer in the vortex sheet model [18, 33, 59]. Moreover, the amplitude of those bands decreases with the lateral position at which the frequency-wavenumber spectrum is represented, following the eigenfunction distribution of the neutral acoustic wave modes S1 given by Tam and Ahuja [59]. Finally, strong components appear along the mode A1 in Figures 22, 23, 24 and 25(a,c,e).

Peak levels are reached in the spectra on the line  $k = -\omega/a_0$ , at the screech Strouhal numbers  $St_{hj} = 0.185$ ,  $St_{hj} = 0.175$ ,  $St_{hj} = 0.115$  and  $St_{hj} = 0.077$  in Figures 22, 23, 24 and 25, respectively. As already observed by the authors in round supersonic screeching jets [18], these tones are located very near the lower limits of the dispersion relations of the neutral acoustic wave modes of the equivalent ideally expanded jet.

Therefore, the associated waves propagate upstream inside the jet with group and phase velocities both close to the ambient speed of sound. In conclusion, at the screech frequencies, acoustic waves propagating in the upstream direction at the ambient speed of sound also exist in the jet flow, additionally to the acoustic waves propagating outside of the jet, as noted by Tam and Hu [57] and by Tam and Ahuja [59]. These acoustic waves belong to the neutral acoustic wave modes of the equivalent ideally expanded jet and explain why, for the simulated screeching rectangular jets, the associated oscillation mode is antisymmetric.

## IX. Conclusions

Implicit LES calculations of a rectangular supersonic jet are conducted for different jet nozzle pressure and temperature ratios. An artificial dissipation mechanism has been implemented in the compressible solver and validated, for enhancing solver's ability in handling such highly compressible flows. The geometry of the nozzle and the exit conditions match those in the experimental study carried out at the University of Cincinnati. However, the jet is initially disturbed in the LES although fully turbulent in the experiments. A convergence study is first performed. Mean fields are found to be in good agreement with experimental results. Four simulations with different temperature ratios are then presented in order to characterize the effect of the temperature on the flow and aeroacoustics of the jets. First, it is shown that the total number of cells in the shock cell structure decreases with the increase of the temperature ratio. However, the temperature ratio does not influence the size of the first shock cell and the linear decrease of the shock cell size in the downstream direction. In case of the shock cell structure, results are found to be similar to those for round non-ideally expanded supersonic jets. The spreading of the jet is characterized by looking at the half velocity widths of the jets along the minor axis and the major axis planes. The jet is observed to spread faster along its minor axis, leading to switch of its major axis downstream. The switchover distance is observed to increase with the temperature ratio. The Overall Sound Pressure Levels are then represented along the minor and major axis planes. It is seen that the intensity of the screech noise increases with the temperature ratio in the present study although the opposite is observed in the experiments. For the higher temperature cases investigated, the strong flapping motion of the jet along the minor axis plane due to the screech feedback mechanism is believed to lead to an asymmetric organization of the Mach wave radiation. Thereafter, the convection velocity of the turbulent structures in the jet shear layers along the minor axis plane is studied. Once normalized by the jet exit velocity, the convection velocity is shown to decrease with the jet temperature ratio, a similar behaviour as observed in round jets. The near- and far-field acoustic fields are studied. In the vicinity of the nozzle, a screech frequency is observed for each jet. This frequency is consistent with both experimental data and a theoretical model. The far-field acoustic fields are computed using a Ffowcs Williams-Hawkings based approach. Four acoustic components typical of non-ideally supersonic jets are observed, namely the screech noise, the broadband shock-associated noise, the mixing noise and the Mach wave noise. Their directivity and frequencies are in agreement with experimental results and models. Finally, the organization of the screech frequency is studied by using a Fourier decomposition of the pressure field. With the increase of the temperature, a change from a flapping motion along the diagonal of the jet to a flapping motion along the minor axis plane of the jet is noted. Finally, the origin of the oscillation mode of the jet associated with the screech noise is investigated on the basis of the hypothesis that the acoustic waves completing the feedback loop in such jets are linked to the upstream-propagating acoustic wave modes of the equivalent ideally expanded planar jets. Using a jet vortex sheet model to describe the dispersion relations of these modes, it is found that this hypothesis allows us to explain the antisymmetric jet oscillation observed in experiments for rectangular screeching jets. It is shown that at the screech frequencies, acoustic waves propagating in the upstream direction at the ambient speed of sound exist also in the jet flow, additionally to the acoustic waves propagating outside of the jet. These acoustic waves belong to the neutral acoustic wave modes of the equivalent ideally expanded jet. These results provide evidences that a vortex sheet model of the corresponding ideally expanded planar jet can be used to predict the wave modes of a non-ideally expanded rectangular supersonic jet. They also suggest that the feedback part of the mechanism causing screech noise in non-ideally expanded rectangular jets is achieved, at least partially, through these waves; explaining why, for the simulated screeching rectangular jets, the associated oscillation mode is antisymmetric.

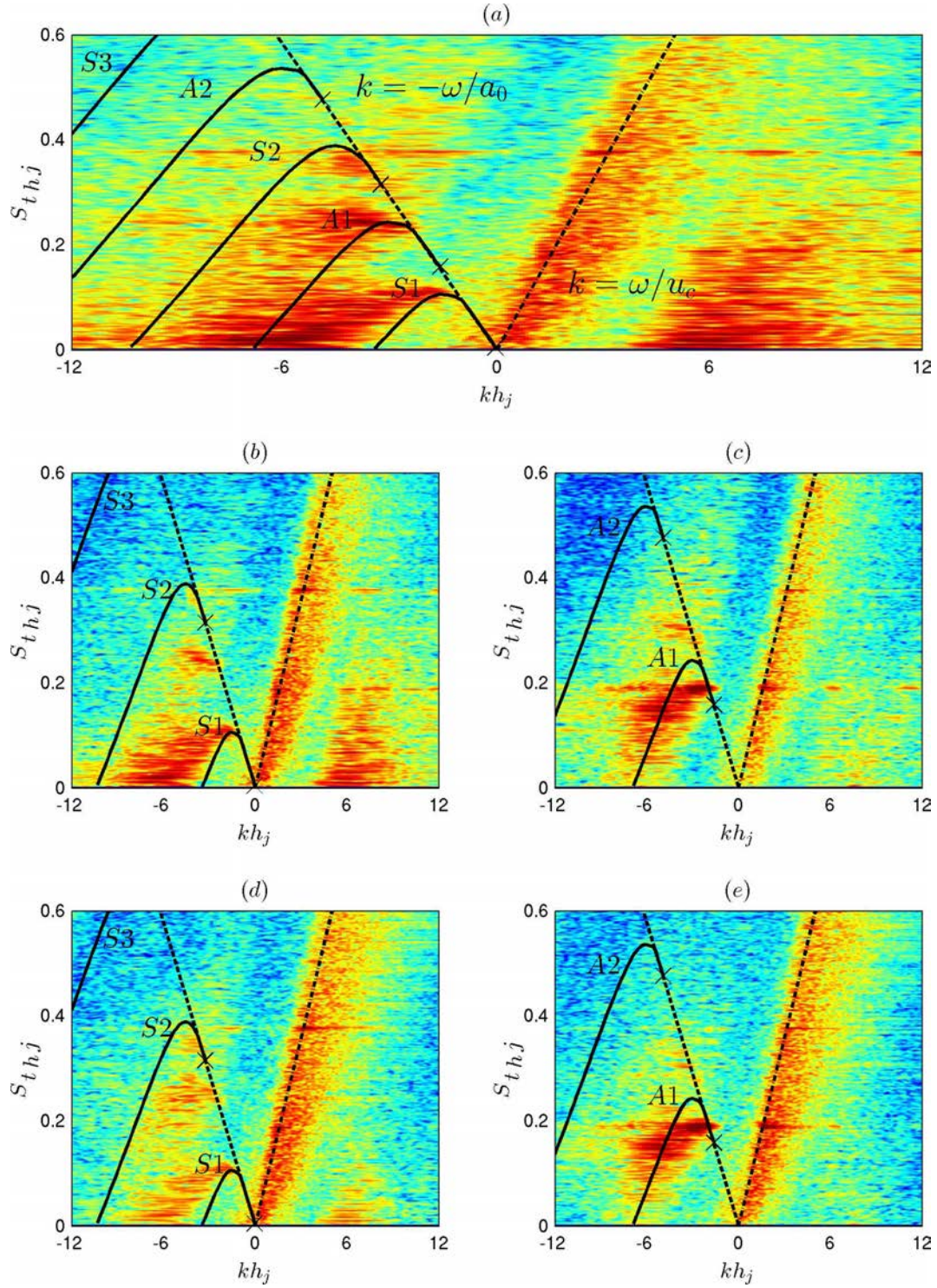


Figure 22. Frequency-wavenumber spectra of pressure fluctuations of the jet with a nozzle pressure ratio of 3 and a temperature ratio of 2 at (a)  $y = 0.1h$ , (b,c)  $y = 0.25h$  and (d,e)  $y = 0.5h$  for the planar modes (b,d)  $n = 0$  and (c,e)  $n = 1$ ; — dispersion relations of (left) the symmetric and (right) the antisymmetric neutral acoustic wave modes for an ideally expanded planar jet at  $M_j = 1.36$ ;  $\times$  lower limits of the modes.



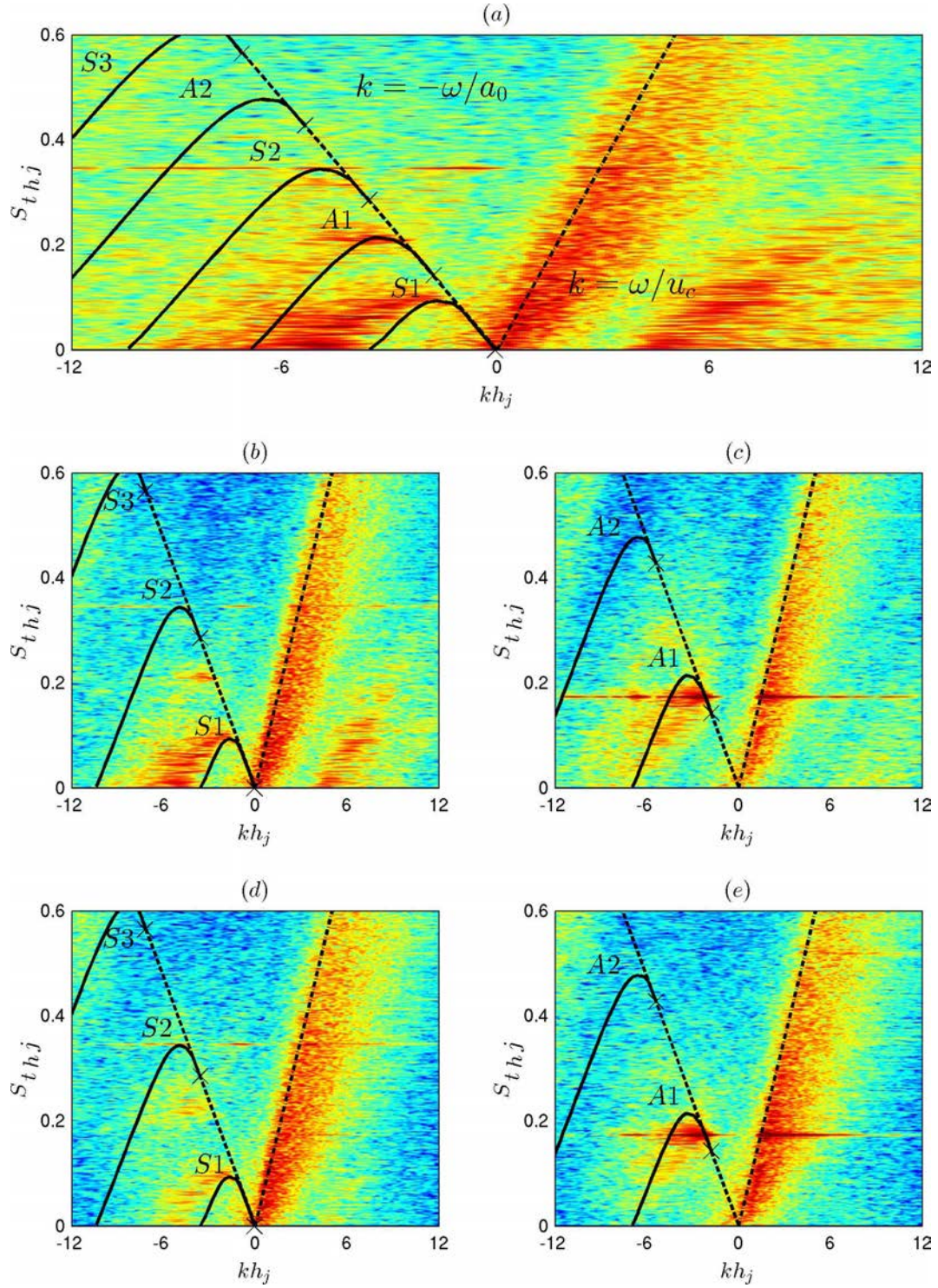


Figure 23. Frequency-wavenumber spectra of pressure fluctuations of the jet with a nozzle pressure ratio of 3 and a temperature ratio of 3 at (a)  $y = 0.1h$ , (b,c)  $y = 0.25h$  and (d,e)  $y = 0.5h$  for the planar modes (b,d)  $n = 0$  and (c,e)  $n = 1$ ; — dispersion relations of (left) the symmetric and (right) the antisymmetric neutral acoustic wave modes for an ideally expanded planar jet at  $M_j = 1.36$ ;  $\times$  lower limits of the modes.

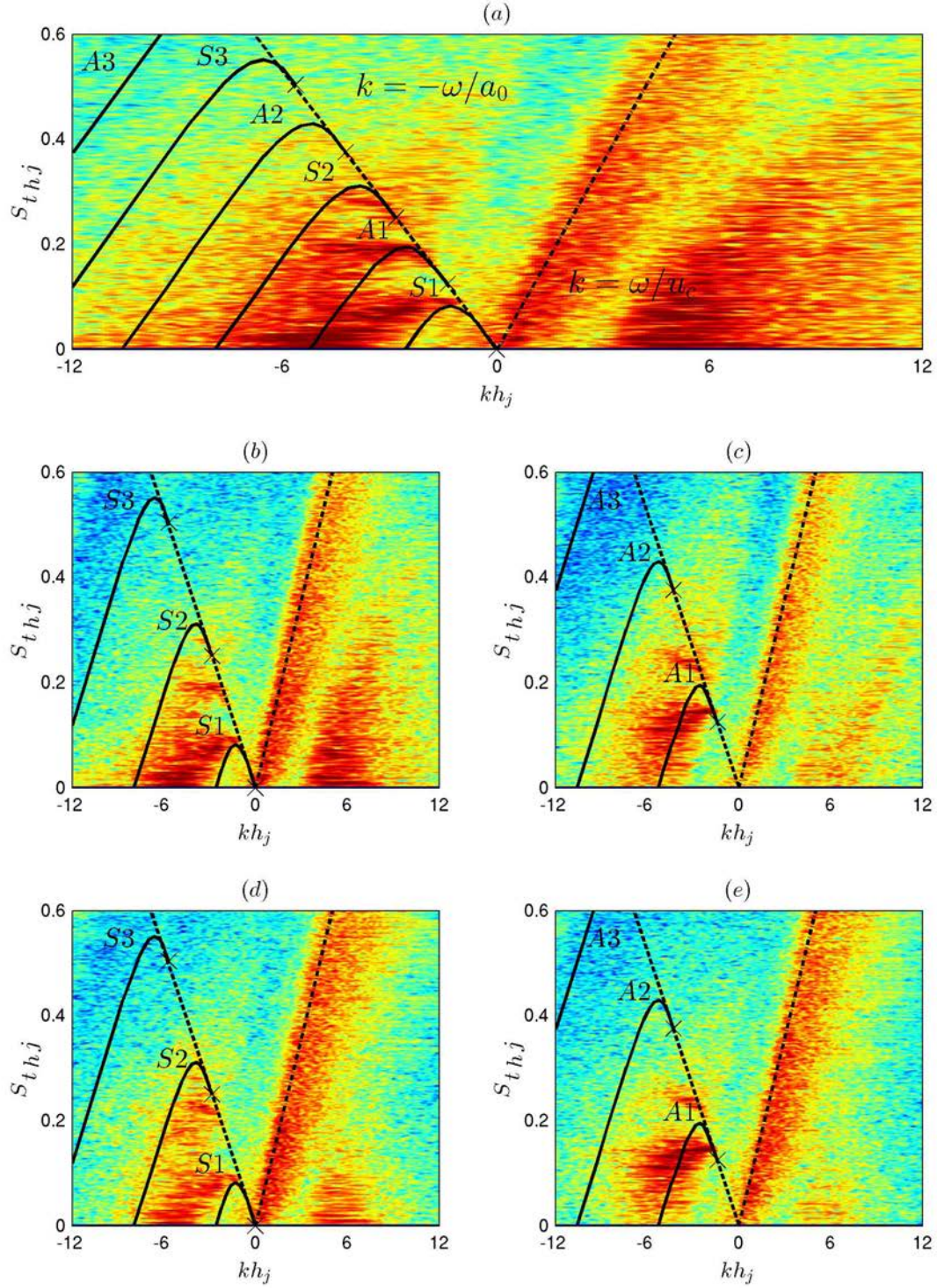


Figure 24. Frequency-wavenumber spectra of pressure fluctuations of the jet with a nozzle pressure ratio of 4 and a temperature ratio of 2 at (a)  $y = 0.1h$ , (b,c)  $y = 0.25h$  and (d,e)  $y = 0.5h$  for the planar modes (b,d)  $n = 0$  and (c,e)  $n = 1$ ; — dispersion relations of (left) the symmetric and (right) the antisymmetric neutral acoustic wave modes for an ideally expanded planar jet at  $M_j = 1.56$ ;  $\times$  lower limits of the modes.



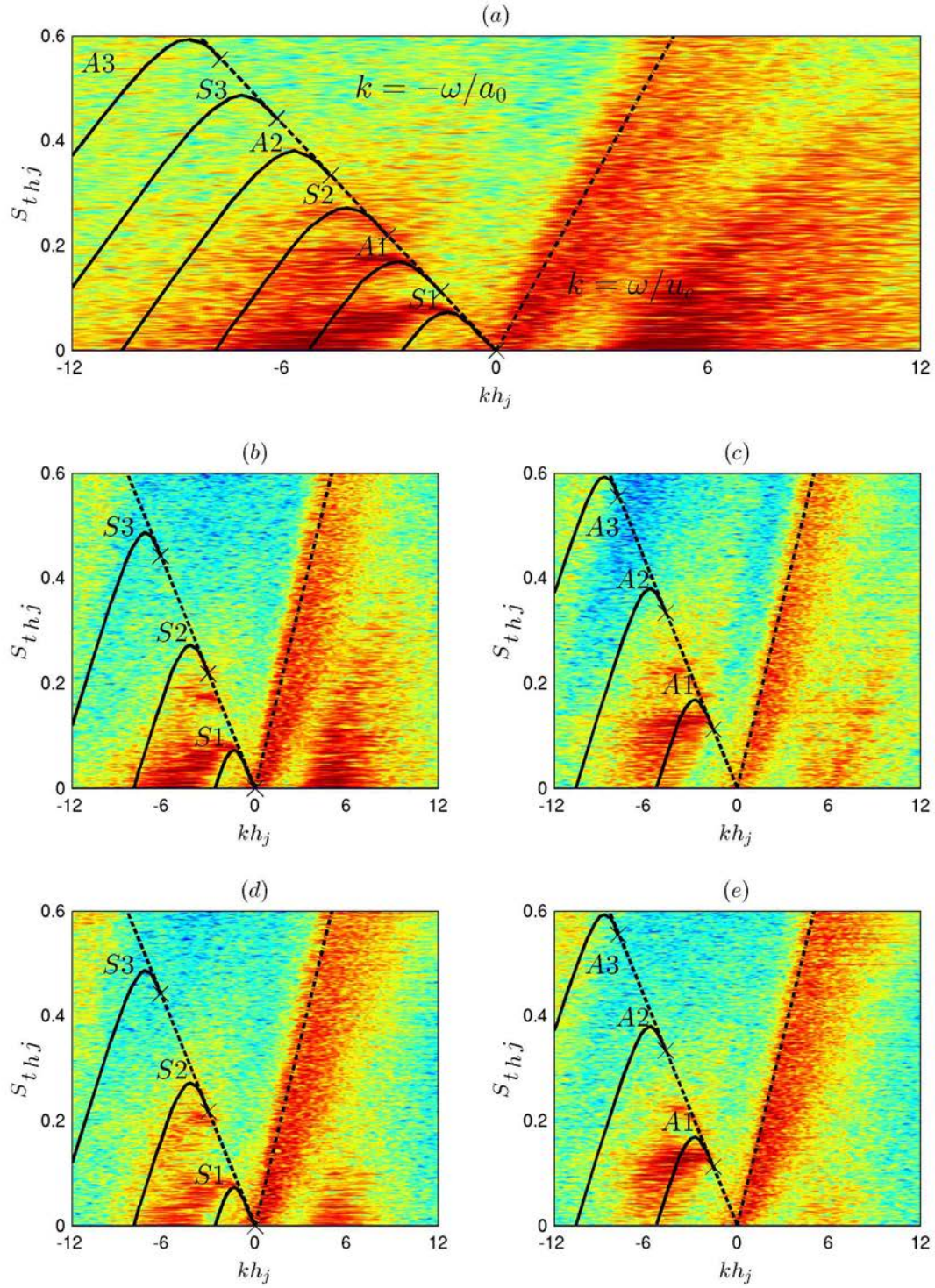


Figure 25. Frequency-wavenumber spectra of pressure fluctuations of the jet with a nozzle pressure ratio of 4 and a temperature ratio of 3 at (a)  $y = 0.1h$ , (b,c)  $y = 0.25h$  and (d,e)  $y = 0.5h$  for the planar modes (b,d)  $n = 0$  and (c,e)  $n = 1$ ; — dispersion relations of (left) the symmetric and (right) the antisymmetric neutral acoustic wave modes for an ideally expanded planar jet at  $M_j = 1.56$ ;  $\times$  lower limits of the modes.

## Acknowledgments

The computations were performed using HPC resources provided by CNRS on Turing, Occigen (GENCI-CINES grant A0042A07178) and Eos (CALMIP, grant 2018-p1425). Florian Baier, PhD at the Department of Aerospace Engineering & Mechanics of the University of Cincinnati is acknowledged for providing the experimental data used in this paper.

## References

- <sup>1</sup> C. Tam, “Supersonic jet noise,” *Annual Review of Fluid Mechanics*, vol. 27, pp. 17–43, 1995. doi: 10.1146/annurev.fl.27.010195.000313.
- <sup>2</sup> E. Gutmark, K. C. Schadow, and C. J. Bicker, “Near acoustic field and shock structure of rectangular supersonic jets,” *AIAA Journal*, vol. 28, no. 7, pp. 1163–1170, 1990. doi: 10.2514/3.25187.
- <sup>3</sup> J. Berland, C. Bogey, and C. Bailly, “Numerical study of screech generation in a planar supersonic jet,” *Physics of fluids*, vol. 19, no. 7, pp. 075105/1–075105/14, 2007. doi: 10.1063/1.2747225.
- <sup>4</sup> C. Bogey and C. Bailly, “Investigation of downstream and sideline subsonic jet noise using large eddy simulation,” *Theoretical and Computational Fluid Dynamics*, vol. 20, no. 1, pp. 23–40, 2006.
- <sup>5</sup> C. Bogey and C. Bailly, “An analysis of the correlations between the turbulent flow and the sound pressure fields of subsonic jets,” *Journal of Fluid Mechanics*, vol. 583, pp. 71–97, 2007. doi: 10.1017/S002211200700612X.
- <sup>6</sup> N. D. Sandham and A. M. Salgado, “Nonlinear interaction model of subsonic jet noise,” *Philosophical Transactions of the Royal Society of London A: Mathematical, Physical and Engineering Sciences*, vol. 366, no. 1876, pp. 2745–2760, 2008. doi: 10.1098/rsta.2008.0049.
- <sup>7</sup> C. K. W. Tam, “Mach wave radiation from high-speed jets,” *AIAA Journal*, vol. 47, no. 10, pp. 2440–2448, 2009. doi: 10.2514/1.42644.
- <sup>8</sup> D. Martlew, “Noise associated with shock waves in supersonic jets. aircraft engine noise and sonic boom,” *AGARD Conference Proceedings*, pp. 1–70, 1969.
- <sup>9</sup> B. André, *Etude expérimentale de l’effet du vol sur le bruit de choc de jets supersoniques sous-détendus*. PhD thesis, Ecole Centrale de Lyon, 2012. 2012–42.
- <sup>10</sup> C. Tam, J. Seiner, and J. Yu, “Proposed relationship between broadband shock associated noise and screech tones,” *Journal of Sound and Vibration*, vol. 110, no. 2, pp. 309–321, 1986. doi: 10.1016/S0022-460X(86)80212-7.
- <sup>11</sup> C. K. W. Tam and H. K. Tanna, “Shock associated noise of supersonic jets from convergent-divergent nozzles,” *Journal of Sound and Vibration*, vol. 81, no. 3, pp. 337–358, 1982. doi:10.1016/0022-460X(82)90244-9.
- <sup>12</sup> M. Harper-Bourne and M. J. Fisher, “The noise from shock waves in supersonic jets,” *AGARD Conference Proceedings*, 1974.
- <sup>13</sup> H. Oertel Sen, *Kinematics of Mach waves inside and outside supersonic jets*. Springer, Berlin, 1979.
- <sup>14</sup> A. Powell, “On the mechanism of choked jet noise,” *Proceedings of the Physical Society. Section B*, vol. 66, no. 12, pp. 1039–1056, 1953.
- <sup>15</sup> G. Raman, “Supersonic jet screech: half-century from powell to the present,” *Journal of Sound and Vibration*, vol. 225, no. 3, pp. 543–571, 1999. doi: 10.1006/jsvi.1999.2181.
- <sup>16</sup> M. Merle, “Sur la fréquence des ondes sonores émises par un jet d’air à grande vitesse,” *Comptes-Rendus de l’Académie des Sciences de Paris*, vol. 243, pp. 490–493, 1956.
- <sup>17</sup> M. G. Davies and D. E. S. Oldfield, “Tones from a choked axisymmetric jet. II. the self excited loop and mode of oscillation,” *Acta Acustica united with Acustica*, vol. 12, pp. 267–277, 1962.



- <sup>18</sup> R. Gojon, C. Bogey, and M. Mihaescu, "Oscillation modes in screeching jets," *AIAA J.*, vol. 56, no. 7, pp. 2918–2924, 2018. doi: 10.2514/1.J056936.
- <sup>19</sup> G. Raman and E. Rice, "Instability modes excited by natural screech tones in a supersonic rectangular jet," *Physics of Fluids*, vol. 6, no. 12, pp. 3999–4008, 1994.
- <sup>20</sup> P. Mora, F. Baier, E. J. Gutmark, and K. Kailasanath, "Acoustics from a rectangular c-d nozzle exhausting over a flat surface," *AIAA Paper 2016-1884*, 2016. doi: 10.2514/6.2016-1884.
- <sup>21</sup> P. Eliasson, *EDGE: A Navier-Stokes solver for unstructured grids*. 2001.
- <sup>22</sup> B. Semlitsch, M. Mihaescu, L. Fuchs, and E. Gutmark, "Analyzing the impact of the inlet temperature on the acoustic noise production from a supersonic jet using large eddy simulations," *Proceedings of Meetings on Acoustics ICA2013*, vol. 19, no. 030011, 2013. doi: 10.1121/1.4799241.
- <sup>23</sup> B. Semlitsch, M. Mihaescu, and L. Fuchs, "Large eddy simulation of fluidic injection into a supersonic convergent-divergent duct," *Direct and Large-Eddy Simulation IX*, pp. 297–302, 2015. doi: 10.1007/978-3-319-14448-1\_37.
- <sup>24</sup> C. Bogey and C. Bailly, "Large eddy simulations of transitional round jets: influence of the reynolds number on flow development and energy dissipation," *Physics of Fluids*, vol. 18, no. 6, p. 065101, 2006. doi: 10.1063/1.2204060.
- <sup>25</sup> F. Kremer and C. Bogey, "Large-eddy simulation of turbulent channel flow using relaxation filtering: Resolution requirement and reynolds number effects," *Computers & Fluids*, vol. 116, pp. 17–28, 2015. doi: 10.1016/j.compfluid.2015.03.026.
- <sup>26</sup> R. Gojon and C. Bogey, "Numerical study of the flow and the near acoustic fields of an underexpanded round free jet generating two screech tones," *International Journal of Aeroacoustics*, vol. 16, no. 7-8, pp. 603–625, 2017. doi: 10.1177/1475472X17727606.
- <sup>27</sup> A. Jameson, W. Schmidt, and E. Turkel, "Numerical solutions of the euler equations by finite volume methods using runge-kutta time-stepping schemes," *AIAA paper 1981-1259*, 1981. doi :10.2514/6.1981-1259.
- <sup>28</sup> F. Ducros, V. Ferrand, F. Nicoud, C. Weber, D. Darracq, C. Gacherieu, and T. Poinso, "Large-eddy simulation of the shock/turbulence interaction," *Journal of Computational Physics*, vol. 152, no. 2, pp. 517–549, 1999. doi: 10.1006/jcph.1999.6238.
- <sup>29</sup> R. Gojon, F. Baier, E. Gutmark, and M. Mihaescu, "Temperature effects on the aerodynamic and acoustic fields of a rectangular supersonic jet," *AIAA paper 2017-0002*, 2017. doi: 10.2514/6.2017-0002.
- <sup>30</sup> J. Nichols, F. Ham, and S. Lele, "High-fidelity large-eddy simulation for supersonic rectangular jet noise prediction," *AIAA paper 2011-2919*, 2011. doi: 10.2514/6.2011-2919.
- <sup>31</sup> C. Bogey, O. Marsden, and C. Bailly, "Influence of initial turbulence level on the flow and sound fields of a subsonic jet at a diameter-based reynolds number of 100000," *Journal of Fluid Mechanics*, vol. 701, pp. 352–385, 2012. doi: 10.1017/jfm.2012.162.
- <sup>32</sup> M. Lorteau, F. Cléro, and F. Vuillot, "Analysis of noise radiation mechanisms in hot subsonic jet from a validated large eddy simulation solution," *Physics of Fluids*, vol. 27, no. 7, p. 075108, 2015. doi: 10.1063/1.4926792.
- <sup>33</sup> C. Bogey and R. Gojon, "Feedback loop and upwind-propagating waves in ideally expanded supersonic impinging round jets," *Journal of Fluid Mechanics*, vol. 823, pp. 562–591, 2017. doi: 10.1017/jfm.2017.334.
- <sup>34</sup> R. Gojon, C. Bogey, and O. Marsden, "Investigation of tone generation in ideally expanded supersonic planar impinging jets using large-eddy simulation," *Journal of Fluid Mechanics*, vol. 808, pp. 90–115, 2016. doi: 10.1017/jfm.2016.628.
- <sup>35</sup> R. Westley and J. H. Woolley, "The near field sound pressures of a choked jet during a screech cycle," *AGARD Conference Proceedings*, vol. 42, pp. 23.1–23.13, 1969.

- <sup>36</sup> J. Panda, “An experimental investigation of screech noise generation,” *Journal of Fluid Mechanics*, vol. 378, pp. 71–96, 1999. doi: 10.1017/S0022112098003383.
- <sup>37</sup> M. Dahl, “Predictions of supersonic jet mixing and shock-associated noise compared with measured far-field data,” *NASA Technical Report*, vol. TM-2010-216328, 2010.
- <sup>38</sup> J. Panda and R. G. Seasholtz, “Experimental investigation of density fluctuations in high-speed jets and correlation with generated noise,” *Journal of Fluid Mechanics*, vol. 450, pp. 97–130, 2002. doi: 10.1017/S002211200100622X.
- <sup>39</sup> J. W. Nichols and S. K. Lele, “Large eddy simulation of crackle noise in hot supersonic jets,” *The Journal of the Acoustical Society of America*, vol. 134, no. 5, pp. 4128–4138, 2013. doi: 10.1121/1.4831161.
- <sup>40</sup> Y. Hsia, A. Krothapalli, D. Baganoff, and K. Karamcheti, “Effects of mach number on the development of a subsonic rectangular jet,” *AIAA Journal*, vol. 21, no. 2, pp. 176–177, 1983. doi: 10.2514/3.8050.
- <sup>41</sup> K. Zaman, “Axis switching and spreading of an asymmetric jet: the role of coherent structure dynamics,” *Journal of Fluid Mechanics*, vol. 316, pp. 1–27, 1996. doi: 10.1017/S0022112096000420.
- <sup>42</sup> A. Krothapalli, D. Baganoff, and K. Karamcheti, “On the mixing of a rectangular jet,” *Journal of Fluid Mechanics*, vol. 107, pp. 201–220, 1981. doi: 10.1017/S0022112081001730.
- <sup>43</sup> E. Gutmark and K. Schadow, “Flow characteristics of orifice and tapered jets,” *Physics of fluids*, vol. 30, no. 11, pp. 3448–3454, 1987. doi: 10.1063/1.866477.
- <sup>44</sup> C. K. W. Tam, J. Jackson, and J. Seiner, “A multiple-scales model of the shock-cell structure of imperfectly expanded supersonic jets,” *Journal of Fluid Mechanics*, vol. 153, pp. 123–149, 1985. doi: 10.1017/S0022112085001173.
- <sup>45</sup> C. K. W. Tam, “The shock-cell structures and screech tone frequencies of rectangular and non-axisymmetric supersonic jets,” *Journal of Sound and Vibration*, vol. 121, no. 1, pp. 135–147, 1988. doi: 10.1016/S0022-460X(88)80066-X.
- <sup>46</sup> B. André, T. Castelain, and C. Bailly, “Investigation of the mixing layer of underexpanded supersonic jets by particle image velocimetry,” *International Journal of Heat and Fluid Flow*, vol. 50, pp. 188–200, 2014. doi: 10.1016/j.ijheatfluidflow.2014.08.004.
- <sup>47</sup> J. Panda, G. Raman, and K. Zaman, “Underexpanded screeching jets from circular, rectangular and elliptic nozzles,” *AIAA Paper 97-1623*, 1997.
- <sup>48</sup> R. Gojon and C. Bogey, “Flow structure oscillations and tone production in underexpanded impinging round jets,” *AIAA Journal*, vol. 55, no. 6, pp. 1792–1805, 2017. doi: 10.2514/1.J055618.
- <sup>49</sup> J. Liu, A. Corrigan, K. Kailasanath, and E. Gutmark, “Effects of temperature on noise generation in supersonic jets,” *AIAA paper 2016-2937*, 2016. doi: 10.2514/6.2016-2937.
- <sup>50</sup> M. Shur, P. Spalart, and M. Strelets, “Noise prediction for increasingly complex jets. part i: Methods and tests,” *International Journal of Aeroacoustics*, vol. 4, no. 3, pp. 213–245, 2005. doi: 10.1260/1475472054771376.
- <sup>51</sup> G. A. Brès, F. E. Ham, J. W. Nichols, and S. K. Lele, “Nozzle wall modeling in unstructured large eddy simulations for hot supersonic jet predictions,” *AIAA paper 2013-2142*, 2013. doi: 10.2514/6.2013-2142.
- <sup>52</sup> D. G. Crighton, A. P. Dowling, J. E. Ffowcs Williams, M. A. Heckl, and F. A. Leppington, *Ffowcs Williams, J. E., Noise Source Mechanisms, in: Modern Methods in Analytical Acoustics: Lecture Notes*. 1992.
- <sup>53</sup> H. D. Yao, L. Davidson, L. E. Eriksson, S. H. Peng, O. Grundestam, and P. E. Eliasson, “Surface integral analogy approaches for predicting noise from 3d high-lift low-noise wings,” *Acta Mechanica Sinica*, vol. 30, no. 3, pp. 326–338, 2014. doi: 10.1007/s10409-014-0008-y.

- <sup>54</sup> G. Raman, "Screech tones from rectangular jets with spanwise oblique shock-cell structures," *Journal of Fluid Mechanics*, vol. 330, pp. 141–168, 1997. doi: 10.1017/S0022112096003801.
- <sup>55</sup> H. Shen and C. Tam, "Three-dimensional numerical simulation of the jet screech phenomenon," *AIAA journal*, vol. 40, no. 1, pp. 33–41, 2002. doi: 10.2514/2.1638.
- <sup>56</sup> C. Tam and T. Norum, "Impingement tones of large aspect ratio supersonic rectangular jets," *AIAA J.*, vol. 30, no. 2, pp. 304–311, 1992.
- <sup>57</sup> C. K. W. Tam and F. Q. Hu, "On the three families of instability waves of high-speed jets," *J. Fluid Mech.*, vol. 201, pp. 447–483, 1989.
- <sup>58</sup> K. A. Alkislar M.B. and L. L.M., "Structure of a screeching rectangular jet: a stereoscopic particle image velocimetry study," *Journal of Fluid Mechanics*, vol. 489, pp. 121–154, 2003. doi: 10.1017/S0022112003005032.
- <sup>59</sup> C. K. W. Tam and K. K. Ahuja, "Theoretical model of discrete tone generation by impinging jets," *J. Fluid Mech.*, vol. 214, pp. 67–87, 1990.
- <sup>60</sup> A. Towne, A. V. G. Cavalieri, P. Jordan, T. Colonius, O. Schmidt, V. Jaunet, and G. Brès, "Acoustic resonance in the potential core of subsonic jets," *Journal of Fluid Mechanics*, vol. 825, pp. 1113–1152, 2017. doi: 10.1017/jfm.2017.346.